

DOI: 10.1002/aenm.201901286

**Article type: Full Paper**

**Multifunctional Solar Waterways: Plasma-enabled Self-cleaning Nano-architectures for Energy-efficient Desalination**

*Shenghao Wu, Guoping Xiong, Huachao Yang, Biyao Gong, Yikuan Tian, Chenxuan Xu, Yan Wang, Timothy Fisher, Jianhua Yan, Kefa Cen, Tengfei Luo, Xin Tu, Zheng Bo\* and Kostya (Ken) Ostrikov*

*S. H. Wu, Dr. H. C. Yang, B. Y. Gong, T. K. Tian, C. X. Xu, Prof. J. H. Yan, Prof. K. F. Cen, Prof. Z. Bo*

State Key Laboratory of Clean Energy Utilization  
College of Energy Engineering, Zhejiang University  
Hangzhou, Zhejiang 310027, China

E-mail: bozh@zju.edu.cn

*Prof. G. P. Xiong, Prof. Y. Wang*

Department of Mechanical Engineering  
University of Nevada  
Reno, Nevada 89557, United States

*Prof. T. Fisher*

Department of Mechanical & Aerospace Engineering and California nanoSystems Institute  
University of California Los Angeles  
Los Angeles, California 90095, United States

*Prof. T. F. Luo*

Department of Aerospace and Mechanical Engineering

University of Notre Dame

Notre Dame, Indiana 46556, United States

*Dr. X. Tu*

Department of Electrical Engineering and Electronics

University of Liverpool

Liverpool, L69 3GJ, UK

*Prof. K. Ostrikov*

School of Chemistry, Physics and Mechanical Engineering

Queensland University of Technology Brisbane, Queensland 4000, Australia

Joint CSIRO-QUT Sustainable Processes and Devices Laboratory

P. O. Box 218, Lindfield, NSW 2070, Australia

State Key Laboratory of Clean Energy Utilization

College of Energy Engineering, Zhejiang University

Hangzhou, Zhejiang 310027, China

**Keywords:** energy conversion materials, plasma nanotechnology, plasma graphene fabrication, water desalination, self-cleaning

Evaporating seawater and separating salt from water is one of the most promising solutions for global water scarcity. State-of-the-art water desalination devices combining solar harvesting and heat localization for evaporation using nanomaterials still suffer from several issues in energy efficiency, long-term performance, salt fouling, light blocking and clean water collection in real-world applications. To address these issues, this work devises plasma-enabled multi-functional all-carbon nano-architectures with on-surface waterways formed by nitrogen-doped hydrophilic graphene nanopetals (N-fGPs) seamlessly integrated onto the external surface of hydrophobic self-assembled graphene foam (sGF). The N-fGPs

simultaneously transport water and salt ions, absorb sunlight, serve as evaporation surfaces, then capture the salts, followed by self-cleaning. The sGF ensures effective thermal insulation and enhanced heat localization, contributing to high solar-vapor efficiency of  $88.6\pm 2.1\%$ . Seamless connection between N-fGPs and sGF and self-cleaning of N-fGPs structures by re-dissolution of the captured salts in the waterways lead to long-term stability over 240 hours of continuous operation in real seawater without performance degradation, and high daily evaporation yield of  $15.76 \text{ kg m}^{-2}$ . By eliminating sunlight blocking and guiding condensed vapor, a high clean water collection ratio of 83.5% is achieved. The multiple functionalities make the current nano-architectures promising as multipurpose advanced energy materials.

## 1. Introduction

Clean water is one of the most important resources for life. The continuously increasing demand for economic development and increasing pollution lead to severe water scarcity in a growing portion of the world.<sup>[1-2]</sup> Desalination based on evaporating seawater and separating salt from water, is one of the most promising solutions for the global water scarcity, yet is still facing major challenges to achieve efficient energy utilization.<sup>[3-5]</sup> A recent report combining solar harvesting and heat localization for evaporation achieved a relatively high energy efficiency over 85%,<sup>[6]</sup> opening up new opportunities for efficient solar desalination. Subsequent works were devoted to improve the evaporation performance by developing structural designs and optimizing light-absorbing and thermal-insulating materials.<sup>[7-15]</sup> However, the state-of-the-art water desalination devices still suffer from several issues in energy efficiency, long-term performance, salt fouling, light blocking and clean water collection in real-world applications.

In typical double-layer structures for solar thermal desalination, a light absorber is stacked on top of a thermal insulator, while water often flows through and fills the interior of the bottom insulators and then reach the top absorber.<sup>[6,16-20]</sup> However, water is a thermally conductive material with high thermal conductivity of  $0.599 \text{ W K}^{-1} \text{ m}^{-1}$ , much higher than the commonly-used thermal-insulating materials (e.g.,  $0.117 \text{ W K}^{-1} \text{ m}^{-1}$  of carbon foam<sup>[6]</sup>,  $0.069 \text{ W K}^{-1} \text{ m}^{-1}$  of bacteria nanocellulose<sup>[16]</sup>, and  $0.016 \text{ W K}^{-1} \text{ m}^{-1}$  of graphene foam<sup>[19]</sup>). The water infiltrating into the insulator will diminish the thermally insulating efficacy and increase heat conduction to the underlying bulk water, resulting in the temperature increase of bulk liquid. Eventually, the heat leakage from the hot liquid to the adjacent environment by conduction, convection and radiation leads to declined energy efficiency. Meanwhile, salts deposition on the surface of the absorber and the interior of the insulator will reduce light absorption and thermal insulation, resulting in deterioration of the evaporation performance and long-term instability.<sup>[21-23]</sup> Moreover, although existing literatures have reported high solar-vapor energy

efficiency (i.e., the proportion of a given quantity of solar energy used for vapor production) over 90%,<sup>[12,22,24-27]</sup> the solar-water energy efficiency (i.e., the proportion of a given quantity of solar energy used for clean water production which is effectively collected) and clean water collection ratio still fall at very low level of 22% and 39.3%,<sup>[21]</sup> respectively, far below the expectations.

Another issue in real-world desalination is related to the white vapor mist filling evaporating systems and the translucent condensation sticking on domes or plates. The vapor mist and condensation will block (partially absorb or reflect) incident light, leading to significant declines of evaporation performance. Meanwhile, the condensed water is hard to be collected and even some fall back to feed liquid in some desalination devices. It leads to inferior water collection performance and low solar-water energy efficiency.<sup>[21]</sup> As such, more works are required to tackle these challenges and simultaneously achieve higher energy efficiency, long-term stability, anti-salt-fouling behavior and improved clean water collection performance.

Here, we demonstrate a concept of plasma-enabled on-surface waterways to address the water-infiltrating and salt-fouling issues, achieving high energy efficiency, long-term stability as well as self-cleaning and anti-salt-fouling performance of the solar desalination devices. As shown in **Figure 1a**, the hydrophilic light-absorbing material is uniformly coated on the external surface of hydrophobic thermal-insulating material with a spatially seamless and mechanically robust connection. The on-surface light-absorbing material captures light and simultaneously serves as water and ion pathways, ensuring sufficient water supply for solar vapor generation and spontaneous salt diffusion for self-cleaning behavior. Meanwhile, the internal thermal-insulating material prevents water infiltration and salt fouling due to its intrinsically hydrophobic nature, maintaining thermally insulating efficacy.

In the current proof-of-concept work, nitrogen doped freestanding graphene nanopetals (denoted as N-fGNs, the light-absorbing material) are directly ingrown from the external

surface of a monolith of self-assembled graphene foam (denoted as sGF, the thermal-insulating material) via one-step plasma enhanced chemical vapor deposition (PECVD) method. The N-fGNs are tightly connected with the scaffolds of sGF by fused junctions, forming an integrated and hierarchical structure (denoted as N-fGN/sGF). Meanwhile, the on-surface N-fGNs presents hydrophilicity while the internal sGF shows hydrophobicity, thereby, enabling on-surface waterways.

The as-fabricated N-fGN/sGF architecture is employed for solar vapor desalination under a normal solar irradiation of  $1 \text{ kW m}^{-2}$  (i.e., 1 sun). As a consequence, the unique construction of on-surface waterways leads to high solar-vapor efficiency of  $88.6 \pm 2.1\%$  and high daily evaporation yield of  $\sim 15.76 \text{ kg m}^{-2}$  with a real-word feed of natural seawater. Moreover, the spatially seamless connection between N-fGNs and sGF, mechanical and thermal stability, as well as the self-cleaning and anti-salt-fouling behavior ensure the excellent durability over 240 hours of continuous operation without performance degradation. By eliminating sunlight blocking and guiding the transport of hot vapor, a high clean water collection ratio of 83.5% is achieved.

## **2. Results and Discussion**

### **2.1. Characterization of the N-fGN/sGF nano-architectures**

Through the one-step PECVD process, as shown in Figure 1a-1d, wall-like N-fGNs are directly deposited on and perpendicularly ingrown from the porous scaffolds of sGF to construct an integrated structure (i.e., N-fGNs/sGF). Assuming light comes from above, the N-fGNs with vertical orientation nearly parallel to the incident light can serve as the light-absorbing material to maximize solar energy harvest. The sGF with porous scaffolds and a large quantity of interspace filled by air can serve as the thermal-insulating material to suppress heat conduction loss. In this way, the two functions of light absorption and thermal insulation are combined into one integrated N-fGNs/sGF architecture.

Figure 1b-1d shows the optical images of the N-fGNs/sGF samples. After the one-step PECVD process, the colour of the surface changes from metallic grey (i.e., sGF) to deep black color (i.e., N-fGNs/sGF), as shown in Figure 1b and 1c. In contrast, the internal portion of N-fGNs/sGF maintains the original metallic grey color (i.e., sGF), as shown by the cross-section view (Figure 1d), indicating that N-fGNs are only deposited on the external surface of sGF. The morphology of N-fGNs/sGF are shown by the scanning electron microscope (SEM) images in Figure 1e-1g. The N-fGNs are densely coated on the porous scaffolds of sGF, leading to a rough surface (see Figure 1e). The high-magnification SEM image in Figure 1f reveals that these graphene nanoarrays with sharp and exposed edges and open micro/nano channels are uniformly distributed on the wrinkled sheets of sGF. The wall-like nanostructures perpendicularly grow from the substrate with a typical thickness of  $\sim 2 \mu\text{m}$  (see the side view in the inset of Figure 1f), which is time-dependent during the PECVD process. The typical span width of a single unwrinkled two-dimensional graphene nanopetal of N-fGNs falls in the range of several hundred nanometres (Figure 1f) which is much smaller than the micro sheets of sGF with several micrometres (Figure 1g). The thickness of a single plasma-made graphene nanopetal is ultrathin with several nanometres, corresponding to 5 to 8 graphitic layers, as shown by the transmission electron microscope (TEM) image in Figure S1a (Supporting Information). Note that the porous scaffolds in the internal portion of sGF are well-preserved in the PECVD process. As shown in Figure 1g, the internal portion of N-fGNs/sGF maintains N-fGNs-free scaffolds and smooth graphene sheets.

In other words, the N-fGNs are selectively deposited on the external portion of sGF as the radicals in the plasma sheath of the PECVD process hardly go inside the sGF frameworks.<sup>[28]</sup> Moreover, the N-fGNs are seamlessly integrated into the host sGF with intrinsically fused junctions (e.g., chemical bonding, see Figure S1b, Supporting Information) which are formed under high temperature ( $700^\circ\text{C}$ ) and energy-intensive plasma sheath.<sup>[28-29]</sup> The stable

chemical bonds connecting N-fGNs and sGF result in a mechanically robust interface, benefiting practical applications.

The plasma-made N-fGNs present hydrophilic wettability, while the internal portion of sGF maintains the intrinsically hydrophobic nature. As shown in **Figure 2a**, when a water droplet interacts with the external surface of N-fGNs/sGF, it rapidly penetrates into the material within a very short time of 4 s. It is suggested that the hydrophilic N-fGNs possessing a large quantity of nano/micro graphene channels can serve as pathways for water transport. On the other hand, when a water droplet drops on the internal portion (i.e., cross-section) of N-fGNs/sGF, it is repelled by the hydrophobic sGF, evidenced by the large water contact angle of 135.4°. Even after 10 s, the water droplet still maintains the large contact angle of 134.1°. Moreover, these wetting responses are well-maintained even under the irradiation with a normal solar density of 1 kW m<sup>-2</sup>. More details are available in Figure S2 (Supporting Information).

Therefore, the unique structure of on-surface waterways is rationally constructed through the one-step PECVD process. It is worth noting that the hydrophilic nature of N-fGNs is attributed to the nitrogen doping effect during the PECVD process because nitrogen doping can significantly change the wettability of graphene.<sup>[30]</sup> In the PECVD process, CH<sub>4</sub> can be decomposed to generate a range of species (e.g., CH<sub>x</sub>, C and C<sub>2</sub>), which serve as the building units for the construction of graphitic structures.<sup>[31]</sup> In particular, C<sub>2</sub> species play a significant role in the synthesis of graphene, especially for the formation of critical nuclei, which has been well demonstrated in previous works [31]. Meanwhile, a variety of nitrogen species (NH, NH<sub>2</sub> and N) generated from the NH<sub>3</sub> containing plasma are inserted into the defects and edges of graphene nanopetals or substitute carbon atoms in the graphitic structures.<sup>[32-33]</sup>

As shown by the X-ray photoelectron spectroscopy (XPS) results in Figure 2c, various nitrogen-containing functional groups are introduced into the freestanding graphitic structures,<sup>[34]</sup> such as pyridinic-N (at 395.4 eV, 15.9%), pyrrolic-N (at 397.4 eV, 44.7%),



graphitic-N (at 399.4 eV, 27.9%) and pyridinic-N-oxide (at 402.8 eV, 11.5%), leading to a dramatically increased nitrogen/carbon atomic ratio of 0.041. Additionally, an oxygen peak with a relatively high oxygen/carbon atomic ratio of 0.069 elevates at 528.6 eV in the XPS spectrum. It is attributed to the oxygen adsorption by the nitrogen-containing groups, and the oxygen-containing groups (e.g., -OH, -COOH) bonding to reactive graphene edges.<sup>[35-36]</sup> The increased oxygen content and hydrophilic oxygen-containing groups also improve the hydrophilic wettability of graphene. More importantly, these nitrogen- and oxygen-containing functional groups are stable when exposing to saline water, evidenced by the well-preserved atom ratios (see Figure S3, Supporting Information).

To demonstrate the efficacy of the as-constructed on-surface waterways, a water wicking test was performed. As schematically shown by the inset of Figure 2d, the evolution of water mass adsorbed by a N-fGNs/sGF sample with a diameter a 4 cm was monitored by a precise balance. When the bottom portion of the N-fGNs/sGF sample contacts with water, the underlying water is adsorbed by the N-fGNs/sGF sample, resulting in the increase of mass. The water wicking evolution, which is obtained by dividing the adsorbed water mass by the section perimeter (ca.  $4 \times \pi \times 10^{-2}$  m) of the N-fGNs/sGF sample (see the detailed method in Section S4, Supporting Information), is presented in Figure 2d. The top surface can be completely wetted by water within a short duration of 100 s because of the enhanced capillary in the hydrophilic nano/micro nanochannels of N-fGNs.

As shown in Figure 2d, the water wicking rapidly intensifies during the first 200 s, and then gradually reaches a plateau at 200~300 s. It is worth noting that due to the intrinsic hydrophobicity of sGF, the underneath water can transport only through the hydrophilic channels of the on-surface N-fGNs. This is why we take the value divided by the sample's perimeter (where N-fGNs are coated) to represent the ability of water supply, which is quite important for solar vapor desalination.

The average water wicking rate from half-saturated to the saturated state (in the duration of 8~124 s) are calculated based on section perimeter. The perimeter water wicking rate is calculated to be  $0.55\pm 0.02 \text{ kg m}^{-1} \text{ h}^{-1}$ . Assuming that all vapor is ideally generated at  $20^\circ\text{C}$  (i.e., the minimum energy used for evaporation without energy cost for temperature increase and sensible heat),<sup>[22]</sup> the upper limit of evaporation rate under normal solar irradiation (i.e., 1 sun) is obtained as  $1.47 \text{ kg m}^{-2} \text{ h}^{-1}$ . Note that the latent heat of phase change of water at  $20^\circ\text{C}$  is  $2,453.3 \text{ kJ kg}^{-1}$ . To ensure sufficient water supply for evaporation, the following **Equation 1** should be satisfied:

$$D \times \pi \times m_{wicking} \geq (D^2 \times \pi/4) \times m_{limit} \quad , \quad (1)$$

where  $D$  denotes the diameter of N-fGNs/sGF sample,  $m_{wicking}$  denotes the perimeter water wicking rate and  $m_{limit}$  denotes the upper limit of area evaporation. Consequently, the maximum diameter of a single N-fGNs/sGF sample is calculated to be  $1.49\pm 0.05 \text{ m}$ . Apparently, the water supply by the 4 cm-diameter N-fGNs/sGF sample in the current work is sufficient for solar vapor desalination at 1 sun. In principle, any permanent hydrophilic finishing of the graphene sheets could be used to fabricate the waterways on the surface. However, the most effective way to do this would be in the same process carried in the same reactor chamber. In this work, the synthesis of fGNs with *in situ* N-doping of fGNs was achieved in the same plasma reactor, offering an effective route for the construction of the surface waterways.

The unique on-surface waterways are constructed to suppress the heat conduction loss, which is directly determined by the thermal conductivity of evaporator during practical operation. The thermal conductivities of N-fGNs/sGF at dry is measured to be  $0.036 \text{ W m}^{-1} \text{ K}^{-1}$ . To simulate the real-world condition where the sample is saturated with water adsorption, the N-fGNs/sGF sample is afloat on the water for 10 min before the measurement of thermal conductivity at wet state. As shown in Figure 2e, a low thermal conductivity at wet state of  $0.135 \text{ W m}^{-1} \text{ K}^{-1}$  is obtained, which is much smaller than that of water ( $0.599 \text{ W m}^{-1} \text{ K}^{-1}$ ). The

change of thermal conductivity ( $0.099 \text{ W m}^{-1} \text{ K}^{-1}$ ) from the dry state to the wet state is much smaller than those of the previous works ( $0.397$ ,  $0.264$  and  $0.335 \text{ W m}^{-1} \text{ K}^{-1}$ ),<sup>[16,37-38]</sup> demonstrating the superiority of the current surface waterway design (see more details in Section S5, Supporting Information).

This result can be attributed to the following factors. First, the intrinsically ultralow thermal conductivity ( $0.036 \text{ W m}^{-1} \text{ K}^{-1}$ ) at dry state of the N-fGNs/sGF sample. The sGF host possesses porous scaffolds and air-filled interspace (see the SEM image in Figure 1g), which prevents the heat conduction inside the structures. Second, the unique on-surface waterways. As mentioned afore, conventional thermal-insulating materials are often hydrophilic and easily fill with water. The infiltrated water becomes a significant heat conduction path, leading to dramatic increases of thermal conductivity even close to the water and thus deteriorated thermally insulating behavior,<sup>[6,19,37-38]</sup> as shown in Table S1 (Supporting Information). In the current work, the on-surface waterways are rationally constructed by integrating hydrophilic absorber and hydrophobic insulator by spatially seamless connection while only a thin layer of water (approx. several microns to millimeters) wets the surface of the N-fGNs/sGF sample. Consequently, the internal insulator (i.e., sGF) can maintain dry frameworks during operation, as shown by the inset of Figure 2e, leading to the well-preserved low thermal conductivity. In the measurements of thermal conductivity, round samples with a diameter of 20 mm are used. For evaporation tests or future applications where the sample size is larger, the thermal conductivity could be smaller than  $0.135 \text{ W m}^{-1} \text{ K}^{-1}$ .

For solar-thermal applications, the ability to capture light and convert it to heat is critical. In the current work, the N-fGNs coated on the external surface of sGF serve as light-absorbing material to harvest solar energy. The reflectance ( $R$ ) and transmittance ( $T$ ) of N-fGN/sGF (with a thickness of  $\sim 10 \text{ mm}$ ) are measured, respectively. The absorbance ( $A$ ) is calculated by the equation ( $A=1-R-T$ ). As shown in Figure 2f, the N-fGNs/sGF presents high light absorption across a wide wavelength of 200 to 2,600 nm, which covers the most

energetic part of the solar spectrum (i.e., ultraviolet-visible-near infrared region). The average absorbance is calculated to be ~98%, which means that only less than ~2% light reflects from or transmits through the N-fGNs/sGF sample. The excellent light-harvesting ability can be attributed to the unique morphology of N-fGNs, including the vertical orientation which is nearly parallel to the direction of incident light as well as the wall-like structures, open channels and exposed edges.<sup>[39]</sup> When incident light reaches the graphene nanoarrays, it is trapped in the nano/micro graphene channels and is then almost completely absorbed after multiple internal reflections. Importantly, the role of plasma in the synthesis can be summarized as follows i) growing fGNs to obtain improved light absorption, ii) doping nitrogen species to achieve hydrophilic wettability, and iii) functionalizing the nanoarchitectures to obtain surface waterways (see more details in Section S6, Supporting Information).

In addition, the mechanical stability is also important for real-world conditions, such as rainstorm and ocean wave. The integrated N-fGN/sGF is highly flexible, as shown by the insets of Figure 2g. A N-fGN/sGF sample (with a diameter of 16 mm and a thickness of 10 mm) is pressed by a 50 g weight. When the weight is lifted, the N-fGN/sGF sample recovers to the original shape. Subsequently, the cyclically compressive performance is quantitatively tested. The compressive strain-stress curves are presented in Figure 2g. The cyclic curves nearly overlap with negligible degradation of stress for 10 loading-unloading cycles under a strain of 50%. The outstanding mechanical robustness of N-fGN/sGF nano-architectures can be attributed to the cross-linked three-dimension (3D) graphene frameworks of sGF with strong inter-sheets interactions (e.g., Vander Waals forces and hydrogen bonds).<sup>[40]</sup> Moreover, the N-fGN/sGF architecture is thermally stable in the atmospheric environment ( $O_2:N_2 = 1:4$ ). As shown by the thermogravimetry curves in Figure S7 (Supporting Information), no weight loss is observed until the temperature increases to ~500°C. The thermal and oxidation stability makes the N-fGN/sGF monolith capable of working stably for long times.

## 2.2. Solar desalination by heat localization

The N-fGN/sGF architecture with uniquely constructed on-surface waterways is employed for solar desalination based on heat localization. The experimental set-up is presented in **Figure 3a**. The N-fGN/sGF sample is afloat on the natural seawater collected from the South China Sea without pre-treatment, and is illuminated by simulated solar irradiation with a normal solar density of  $1 \text{ kW m}^{-2}$ . The underlying seawater flows through the on-surface pathways (i.e., the micro/nano channels of N-fGNs) to the top surface of N-fGN/sGF, as shown in **Figure 1a**. The top N-fGNs capture light and convert it to thermal energy. As shown by the Infrared (IR) images in the insets of **Figure 3b**, the top surface temperature of N-fGN/sGF increases rapidly and subsequently form a localized hot region due to the superior light absorption and excellent thermal insulation. The thin layer of water surrounding N-fGNs is heated, and evaporates by liquid-vapor phase change. The temperature evolutions of the vapor (5 mm above the N-fGN/sGF sample) and the water (5 mm below the N-fGN/sGF sample) are monitored by thermocouples.

As shown in **Figure 3b**, the vapor temperature rapidly elevates to  $29.2^\circ\text{C}$  within one minute while the water temperature maintains at an initial temperature of  $20.1^\circ\text{C}$ . Then, the vapor temperature increases slowly and eventually fluctuates at  $33.6 \pm 0.2^\circ\text{C}$ . During the two-hour-long illumination, the water temperature gradually increases to  $22.4^\circ\text{C}$ , corresponding to a small temperature increase of  $2.3^\circ\text{C}$ . This result reveals that only a small amount of heat dissipates to the underneath bulk water and the heat conduction loss is dramatically suppressed.

The evaporation flux is monitored by the precise microbalance. As shown in **Figure 3c**, clean vapor continuously generates and reach a high yield of  $\sim 15.76 \text{ kg m}^{-2}$  after the consecutive operation of 12 hours. Note that only  $\sim 0.43 \text{ kg m}^{-2}$  of clean vapor is contributed to the natural evaporation in dark environment. The average evaporation rate of each hour is

obtained by fitting the evaporation flux and then subtracting the natural evaporation rate of  $0.04 \text{ kg m}^{-2} \text{ h}^{-1}$ . The solar-vapor efficiency is calculated based on the following **Equation 2**:

$$\eta_{\text{solar-vapor}} = m_{\text{evap}} (h_{lv} + C (T_v - T_l)) / q_i \quad , \quad (2)$$

where  $m_{\text{evap}}$  is the evaporation rate,  $h_{lv}$  is the temperature-dependent latent heat ( $2421.1 \text{ kJ kg}^{-1}$  at  $33.6^\circ\text{C}$ ) of phase change,  $C$  is the specific heat of water ( $4.2 \text{ kJ kg}^{-1} \text{ K}^{-1}$ ),  $T_v$  is the temperature of vapor ( $33.6^\circ\text{C}$ ),  $T_l$  is the initial temperature of water ( $20.1^\circ\text{C}$ ), and  $q_i$  is the incident solar energy (i.e.,  $1 \text{ kW m}^{-2}$ ).

As shown in Figure 3d, the evaporation rate continuously increases in the first three hours and saturates at the fourth hour. A small decline of evaporation can be seen after the eighth hour, which might be caused by salt deposition and will be detailedly discussed in the following section. The average evaporation rate over 12 hours is calculated to be  $1.27 \pm 0.03 \text{ kg m}^{-2} \text{ h}^{-1}$ , corresponding to a high solar-vapor efficiency of  $88.6 \pm 2.1\%$ .

The as-obtained high solar-vapor efficiency can be attributed to the following reasons. First, the superior light absorption across a wide wavelength maximizes the solar energy harvesting. More than 98% of incident light is captured by the N-fGNs due to the vertical orientation, wall-like arrays, open channels and exposed edges.

Second, the on-surface waterways together with the intrinsically ultralow thermal conductivity of N-fGN/sGF reduce the heat conduction loss from the top hot region to the underlying bulk liquid. Unlike the water transporting through the entire bottom thermal-insulating materials in conventional double-layer structures, the underneath water can flow only through the on-surface pathways (i.e., the nano/micro channels of N-fGNs) while the internal portion of N-fGN/sGF repels water and keep the dry state even submerged in water. The presence of the water-free sGF layer is further confirmed by the long-time test of water contact angle and water adsorption test in Figure S8 (Supporting Information). Therefore, the heat conduction paths are rationally reduced, resulting in the decreased heat conduction loss

and improved heat localization. According to the thermal analysis (see the detailed method in Section S9, Supporting Information), only 3.0% of energy dissipates to the underneath bulk water through the top-down heat conduction ( $Q_{Conduction}$ ) in N-fGN/sGF, as shown by the inset of Figure 3d. In addition, 2.8% of the heat dissipates by convection ( $Q_{Convection}$ ) while 1.8~10% dissipates by radiation ( $Q_{Radiation}$ ) to surroundings (the hot vapor or the ambient air).

Third, the unique morphology of N-fGNs enhances heat transfer at the solid-liquid interface. The fin-like structures (see the SEM image in Figure 1f) and the ultrathin thickness of a single graphene nanosheet (ca. 1~3 nm, see the TEM images in Figure S1, Supporting Information) of N-fGNs can provide a large quantity of effective area contacting with water for heat exchange. Thus, the thermal energy converted from the absorbed solar energy can transfer through the N-fGNs-water interfaces efficiently. The thin layer of water surrounding N-fGNs can reach a temperature (33.6°C, the vapor temperature measured by thermocouple) much close to the surface temperature of N-fGNs (36.4°C, measured by the IR camera), as shown in Figure 3c.

Fourth, the unique morphology of N-fGNs can accelerate the evaporation process. The hydrophilic surface together with the vertically-oriented graphene arrays stretched the thin layer of water as concave meniscus, which we have previously discussed.<sup>[15,41]</sup> The high-density and sharp graphene edges (demonstrated by the SEM image in Figure 1f and the Raman result in Section S10, Supporting Information) can provide a large number of tips at the three phase (solid-liquid-air) contact lines, where enhanced escape rate of water molecules is obtained. Thus, the evaporation process is accelerated by N-fGNs.

Subsequently, the concentrations of several typical ions in the condensed water collected from the as-generated vapor are measured. As shown in Figure 3e, the ion concentrations in the condensed water dramatically decreases due to the distilling process while these ions are captured by N-fGNs. Quantitatively, the ion concentrations of Na<sup>+</sup>, Mg<sup>2+</sup>, K<sup>+</sup>, Ca<sup>2+</sup> and B<sup>3-</sup> decrease from 6,331, 1,177, 413, 311 and 9.6 mg L<sup>-1</sup> to 8.18, 1.22, 1.25, 1.11 and 0.29 mg L<sup>-1</sup>,

respectively, which obviously reach the World Health Organization (WHO) drinking water standards (i.e., the total dissolved solids of  $\text{Na}^+$ ,  $\text{Mg}^{2+}$ ,  $\text{Ca}^{2+}$  and  $\text{B}^{3-}$  are 200, 25, 100 and 2.4  $\text{mg L}^{-1}$ ),<sup>[42-43]</sup> There is currently no specific WHO guideline value for potassium. Moreover, the durability of the current N-fGN/sGF nano-architectures is tested for over 240 hours. To simulate the real-world working condition (the alternation of day and night), the N-fGN/sGF consecutively works for 12 hours and then naturally afloat on seawater in a dark environment for 12 hours, composing one operation cycle (i.e., one day).

As shown in Figure 3f, the evaporation rate and the solar-vapor efficiency are fluctuating, but no obvious declines in performance are observed over 10 cycles (i.e., 10 days). More importantly, the SEM image in the inset of Figure 3f reveals that the hierarchical morphology and 3D frameworks are well-maintained after 240 hours of operation. Note that the sample was cleaned up by deionized water before the SEM measurement. More discussion is available in Section 11 (Supporting Information). These results thus demonstrate the excellent durability and long-term stability of the integrated N-fGN/sGF nano-architectures, which is very promising for practical applications. On the other hand, the solar desalination performance could be influenced by the saline concentration. The test of solar vapor performance under different salt concentration ranged from 3.25% to 16.25% indicates that the evaporation rate and energy efficiency decrease when increasing the saline concentration. More details are available in Section S12 (Supporting Information). Thus, to obtain stable performance, the seawater in the desalination device was periodically renewed by a peristaltic pump.

### 2.3. Salt deposition and self-cleaning

In practical operations of solar vapor desalination, non-volatile salts usually reside on the holes and surface of evaporators when water directly evaporates from the evaporating system. The salt residues often with white color will reduce the light absorption due to the light



reflection from the salt crystals, and increase the interfacial thermal resistance between light-absorbing materials and water, leading to deteriorated evaporation performances.<sup>[21-23]</sup> Indeed, a small decline in one cycle (i.e., the consecutive operation of 12 hours) especially after the eighth hour is observed (see Figure 3d and 3f), which might be caused by the salt deposition on the top surface of N-fGNs/sGF.

As shown in **Figure 4a**, the salt residues (i.e., the white crystal in red cycles) on the top surface of N-fGNs/sGF can be seen at the sixth hour and then continuously grows as time evolves. Nevertheless, when the light is turned off, the salt residues gradually disappear (Figure 4b). It is because the as-formed salt crystals redissolve into the bulk liquid. Particularly, when the N-fGNs/sGF sample has been naturally afloat on seawater for 9 to 12 hours, almost no salt residue can be seen on the top surface, indicating the self-cleaning ability. This observation explains the recovery of evaporation rate and solar-vapor efficiency after 12 hours of the self-cleaning process, and the long-term stability (see Figure 3f).

The self-cleaning process can be mainly attributed to the spontaneous ion diffusion driven by the salt gradient. Under illumination, the salts captured by the top N-fGNs result in increased ion concentrations over the underneath natural seawater. Meanwhile, the accumulated ions at the top surface of N-fGNs/sGF continuously diffuse through the waterways to the underlying bulk liquid. Thus, the on-surface waterways constructed in the current work can not only transport water but also transport ions. Note that ions diffuse over 24 hours when the evaporation only occurs during daylight hours (12 hours). Based on the diffusion mechanism described by the Fick's law,<sup>[21]</sup> to achieve the self-cleaning performance and avoid salt accumulating at the top surface of the sample, the following **Equation 3** should be satisfied:

$$A_{dif} D_{ion} \rho_{water} (C_{evap} - C_{\infty}) l_w^{-1} t_{dif} \geq A_{evap} m_{vapor} C_{\infty} (1 - C_{\infty})^{-1} t_{evap} \quad , \quad (3)$$

where  $A_{dif}$  is the area for salt diffusion,  $D_{ion}$  is the ion diffusion coefficient (taking the diffusion coefficient of NaCl of  $7.16 \times 10^{-6} \text{ m}^2 \text{ h}^{-1}$  for example),  $\rho_{water}$  is the density of seawater ( $1.04 \times 10^3 \text{ kg m}^{-3}$ ),  $C_{evap}$  is the salinity at the top surface of evaporator (taking the maximum solubility of NaCl of 36 wt% in water at  $20^\circ\text{C}$ ),  $C_\infty$  is the salinity of natural seawater (3.4 wt%),  $l_w$  is the thickness of evaporator ( $10^{-2} \text{ m}$ ),  $t_{dif}$  is the diffusion time (24 hours),  $A_{evap}$  is the area for evaporation ( $4 \times 10^{-4} \pi \text{ m}^2$ ), and  $m_{vapor}$  is evaporation rate ( $1.27 \text{ kg m}^{-2} \text{ h}^{-1}$ ). Consequently, the relation of  $A_{dif} \geq 0.092 A_{evap} \approx 1.16 \times 10^{-4} \text{ m}^2$  is obtained.

However, in the current on-surface waterways, the cross-section area (i.e.,  $A_{dif} = 4 \times 10^{-2} \pi \times h_{nano}$ ) is calculated to be  $2.5 \times 10^{-7} \text{ m}^2$ , where the  $h_{nano}$  denotes the thickness of the plasma-made graphene nanopetals ( $\sim 2 \text{ }\mu\text{m}$ , as shown by the side view of N-fGNs in Figure 1f). Apparently, the as-calculated  $A_{dif}$  does not satisfy the requirement of the diffusion equations. One possible explanation is that a water layer with a thickness from several microns to millimeters covers the surface of graphene micro/nano channels, which directly increase the cross-section area of waterways and thus the area for salt diffusion (i.e.,  $A_{dif}$ ).

Moreover, in real-world conditions, the ocean wave and wind will accelerate the salt diffusion process, benefiting the self-cleaning behavior. The thickness of the plasma-constructed micro/nano pathways can be further elevated by prolonging the PECVD duration, which we have discussed in our previous work.<sup>[44]</sup> The effect of the thickness of N-fGNs is discussed in details in Section S13 (Supporting Information). Importantly, the commonly used anti-salt-fouling methods such as rinsing,<sup>[45]</sup> dipping,<sup>[46]</sup> and coating,<sup>[23]</sup> applied in previous works are not needed for the current N-fGNs/sGF nano-architectures. In addition, salts only deposit on the external surface of N-fGNs/sGF (Figure 4c), while its internal portion always maintains dry and clean (Figure 4d), which is established by the unique construction of on-surface waterways. The ion-containing seawater is repelled by the hydrophobic thermal-insulating material (i.e., sGF). Therefore, the deterioration of thermal insulation caused by salt fouling has been eliminated.

The self-cleaning and anti-salt-fouling behavior of on-surface waterways have addressed the salt-fouling issues, suggesting a potential for long-term and autonomous solar desalination systems. It is worth noting that the saline concentration of the water will increase when the device is in operation. The increasing saline concentration will reduce the speed of ion diffusion and the self-cleaning effect (see Figure S13 and Figure S14, Supporting Information). One solution is to renew the water thus avoiding the increase of the saline level. As such, rational water flow design is necessary to ensure the self-cleaning behavior in real-world applications. In the current work, a water peristaltic pump was employed to renew the water in the desalination device.

#### **2.4. Clean water collection and light blocking**

Clean water collection is very important but challenging for solar vapor desalination. In previous systems, the hot vapor often condenses on a transparent plate/dome and then naturally falls down under gravity,<sup>[4,13,46-47]</sup> as shown in Figure 4e. However, not all condensation is easily collectable, in which lots of condensed droplets stick on the plate/dome wall and even fall back to the bulk liquid. Although the previously reported solar-vapor efficiency can be over 90%,<sup>[12,22,24-27]</sup> the clean water collection ratio still falls at 39.3%,<sup>[21]</sup> corresponding to a very low solar-water efficiency of 22% far below the expectations. Meanwhile, the vapor collection systems (i.e., the plate and dome) stifle the free diffusion of hot vapor. As a result, vapor mist forms inside the evaporating systems, as shown in Figure 4f. The vapor mist and the condensed droplets will block (partially absorb or reflect) the incident light, leading to solar energy loss and thus significantly reduce the evaporation performance.

A reasonable solution is to extract the vapor out of the evaporation systems and then collect it to simultaneously address the light blocking and collection issues. In the current work, an exhaust fan is employed to guide the vapor out the dome, as shown in Figure 4g. For comparison, the tests with the fan turning on and turning off is conducted, respectively. As

shown in Figure 4f, when the fan turns off, white vapor mist fills the dome and droplets condense on the dome wall after only one-hour evaporation at 1 sun. With 12-hour consecutive operation, only  $6.49 \text{ kg m}^{-2}$  of clean water is collected, corresponding to the recycling of 41.2% of hot vapor, which is comparable to previous report (39.3%). On the other hand, when the fan is turned on, the dome always keeps mist- and droplet-free even with 12-hour consecutive evaporation, as shown in Figure 4h. The hot vapor is guided by the exhaust fan into a cooling tube and then the condensation is effectively collected. Note that the exhaust fan could be powered by photovoltaic panels and the thermal energy released by the hot vapor could be recycled, which will be subjects in our future works. As a consequence, the clean water collection dramatically increases to  $13.23 \text{ kg m}^{-2}$ , corresponding to a very high clean water collection ratio of 83.5% and a high solar-water efficiency of 74.0%.

### 3. Conclusion

Water infiltration, salt fouling, light blocking and poor water collection remain significant challenges in solar vapor desalination. This work reports a unique structure of on-surface waterways by directly depositing hydrophilic N-fGPs on the external surface of hydrophobic sGF via the one-step plasma-enabled method, forming an integrated and hierarchical nano-architecture. The wall-like N-fGPs with micro/nano channels are seamlessly ingrown on the external surface of sGF and serve as waterways while the internal sGF repels water infiltrating. The N-fGPs present high light absorbance of 98% across a wide wavelength range from 200 to 2,600 nm due to the vertical orientation, uniform nanoarrays and high-density edges. The sGF possesses an ultralow thermal conductivity of  $0.036 \text{ W m}^{-1} \text{ K}^{-1}$  due to the formation of highly porous frameworks and the air-filled interspace. The uniquely constructed on-surface waterways contribute to the well-maintained thermal insulation (low thermal conductivity of  $0.135 \text{ W m}^{-1} \text{ K}^{-1}$  during operation), long-term stability as well as self-cleaning and anti-salt-fouling performance.

Importantly, high solar-vapor efficiency of  $88.6\pm 2.1\%$  and high daily evaporation yield of  $15.76 \text{ kg m}^{-2}$  are achieved, which are attributed to the superior solar absorption, outstanding thermal insulation and accelerated evaporation process enhanced by the plasma-made fin-like nanostructures and high-density graphene edges. The stable performance is demonstrated over 240 h and can be attributed to the spatially seamless connection between N-fGPs and sGF, mechanical and thermal stability, as well as the self-cleaning and anti-salt-fouling behavior, in which the salt residues captured by N-fGPs during evaporation spontaneously diffuse through the on-surface pathways. By eliminating sunlight blocking and guiding the transport of hot vapor, a high clean water collection ratio of 83.5% and a high solar-water efficiency of 74.0% are achieved. The multiple functionalities make the all-carbon nano-architectures promising as multipurpose advanced energy materials.

#### 4. Experimental section

*sGF fabrication:* sGF was fabricated by a modified hydrothermal method using the precursor of graphene oxide (GO). GO was ultrasonically dispersed in deionized water with  $4 \text{ mg mL}^{-1}$  and magnetically stirred for 1 h. The GO solution was transferred into a Teflon autoclave. The autoclave was heated up to  $120^\circ\text{C}$  by 30 min, subsequently maintained for 10 hours, and then naturally cooled down to the room temperature of  $20^\circ\text{C}$ . The as-obtained product was dialyzed in ethanol solution ( $\text{C}_2\text{H}_6\text{O}$ , 10 vol%) for 6 hours. Finally, sGF was obtained by a freeze-drying process. The as-used GO was synthesized by a modified Hummer's method. In a typical procedure, 1 g natural graphite powder (350 mesh, XFNANO Materials Tech) and 25 mL concentrated sulfuric acid (Sinopharm Chemical Reagent) were mixed and magnetically stirred for 10 min in a  $0^\circ\text{C}$  ice bath. 3.5 g potassium permanganate (Sinopharm Chemical Reagent) was slowly added into the mixture (about 2 hours). Subsequently, the mixture was heated to  $35^\circ\text{C}$  in a water bath and stirred for 2 hours, followed by adding 100 mL deionized water. Then, 8 mL hydrogen peroxide solution (30

wt.% aqueous solution, Sinopharm Chemical Reagent) was slowly added. The product was obtained by centrifugation (8,000 r.m.p., 10 min). Deionized water was used to wash the product and remove the salt and acid residues and repeated for four times. Finally, the GO was obtained by the freeze-drying process.

*N-fGN synthesis:* The N-fGNs were synthesized by a customized inductively coupled plasma enhanced chemical vapor deposition (ICP-PECVD) system. The sGF was used as the substrate for N-fGN growth. In a typical procedure, the sGF substrate was placed in a sealed cylindrical quartz tube, vacuumized to <10 Pa and heated to 700°C in 30 min. A mixture of CH<sub>4</sub> (5 mL min<sup>-1</sup>) and NH<sub>3</sub> (10 mL min<sup>-1</sup>) was used as the gas feed and the pressure in the tube was maintained at ~100 Pa. Subsequently, a radio frequency source of 250 W was coupled into the quartz tube. After one-hour synthesis, the sample was cooled down to room temperature under the protection of 10 mL min<sup>-1</sup> NH<sub>3</sub>, and finally the N-fGN/sGF sample was obtained.

*Materials characterization:* Morphology was characterized by scanning electron microscope (SU-70, Hitachi) and transmission electron microscope (JEM 2100F, JEOL). The photonic transmittance ( $T$ ) and reflectance ( $R$ ) were measured by ultraviolet-visible-near infrared spectrophotometer (UV-3150, Shimadzu), in which an integrating sphere was used. Photonic absorbance ( $A$ ) was calculated by  $A=I-T-R$ . The elemental compositions were measured by Raman microscope (inVia, Renishaw) and X-ray photoelectron spectroscopy (Escalab Mark II, VG) with a monochromatic Mg Ka X-ray source (1,253.6 eV). Thermal conductivity was measured by Hot Disk apparatus (TPS 2500 S, Hot Disk). Thermogravimetry analysis was conducted under simulated air flow (O<sub>2</sub>:N<sub>2</sub> = 1:4) from 50~700°C (Q500, TA).

*Solar vapor desalination test:* A solar simulator (PLS-SXE300D, Beijing Perfect Light Technology) with a <5° collimated output was used as a light source. An optical filter was applied to obtain standard AM 1.5G spectrum. The solar density is measured by an optical

power meter (PL-MW2000, Beijing Perfect Light Technology). The mass change during evaporation was measured using a precision balance (CPA225D, Sartorius) with an accuracy of 0.01 mg. A thermocouple (with an accuracy of 0.01 °C) was placed ~5 mm above the top surface of samples to measure the temperature of the vapor. Two thermocouples were placed in water ~5 mm and 15 mm below the bottom surface of samples, respectively, to indicate the temperature of bulk water. An infrared camera (T1050sc, FLIR) was used to measure the surface temperature of samples. All tests were conducted at atmospheric pressure and ambient temperature (~20°C), with a humidity of ~48%. Error analysis is conducted with multiple sets of repeatable tests.

### **Supporting Information**

Supporting Information is available from the Wiley Online Library or from the author.

### **Acknowledgements**

S. H. Wu, Prof. G. P. Xiong and Dr. H. C. Yang contributed equally to this work. This work is supported by the National Natural Science Foundation of China (No. 51576175) and Zhejiang Provincial Natural Science Foundation of China (No. LR17E060002). Prof. Z. Bo thanks the National Program for Support of Top-notch Young Professionals. Prof. G. P. Xiong and Prof. Y. Wang would like to acknowledge the financial support by the start-up funding from the University of Nevada, Reno. Prof. K. Ostrikov thanks the Australian Research Council for partial support.

### **Conflict of Interest**

The authors declare no conflict of interest.

Received: ((will be filled in by the editorial staff))

Revised: ((will be filled in by the editorial staff))

Published online: ((will be filled in by the editorial staff))

## References

- [1] F. Pulizzi, W. Sun, *Nat. Nanotech.* **2018**, *13*, 633.
- [2] P. Westerhoff, A. Atkinson, J. Fortner, M. S. Wong, J. Zimmerman, J. Gardea-Torresdey, J. Ranville, P. Herckes, *Nat. Nanotech.* **2018**, *13*, 661.
- [3] L. Zhou, Y. Tan, J. Wang, W. Xu, Y. Yuan, W. Cai, S. Zhu, J. Zhu, *Nat. Photonics* **2016**, *10*, 393.
- [4] P. Zhang, J. Li, L. Lv, Y. Zhao, L. Qu, *ACS Nano* **2017**, *11*, 5087.
- [5] O. Neumann, A. S. Urban, J. Day, S. Lal, P. Nordlander, N. J. Halas, *ACS Nano* **2013**, *7*, 42.
- [6] H. Ghasemi, G. Ni, A. M. Marconnet, J. Loomis, S. Yerci, N. Miljkovic, G. Chen, *Nat. Commun.* **2014**, *5*, 4449.
- [7] X. Li, W. Xu, M. Tang, L. Zhou, B. Zhu, S. Zhu, J. Zhu, *Proc. Natl. Acad. Sci. U.S.A.* **2016**, *113*, 13953.
- [8] H. Liu, C. Chen, G. Chen, Y. Kuang, X. Zhao, J. Song, C. Jia, X. Xu, E. Hitz, H. Xie, S. Wang, F. Jiang, T. Li, Y. Li, A. Gong, R. Yang, S. Das, L. Hu, *Adv. Energy. Mater.* **2018**, *8*, 1701616.
- [9] L. Zhu, M. Gao, C. K. N. Peh, X. Wang, G. W. Ho, *Adv. Energy. Mater.* **2018**, *8*, 1702149.
- [10] T. Li, H. Liu, X. Zhao, G. Chen, J. Dai, G. Pastel, C. Jia, C. Chen, E. Hitz, D. Siddhartha, R. Yang, L. Hu, *Adv. Funct. Mater.* **2018**, *28*, 1707134.
- [11] F. Liu, B. Zhao, W. Wu, H. Yang, Y. Ning, Y. Lai, R. Bradley, *Adv. Funct. Mater.* **2018**, *28*, 1803266.
- [12] F. Zhao, X. Zhou, Y. Shi, X. Qian, M. Alexander, X. Zhao, S. Mendez, R. Yang, L. Qu, G. Yu, *Nat. Nanotech.* **2018**, *13*, 489.
- [13] L. Yi, S. Ci, S. Luo, P. Shao, Y. Hou, Z. Wen, *Nano Energy* **2017**, *41*, 600.
- [14] Y. Li, T. Gao, Z. Yang, C. Chen, Y. Kuang, J. Song, C. Jia, E. M. Hitz, B. Yang, L. Hu, *Nano Energy* **2017**, *41*, 201.



- [15] J. Yang, Y. Pang, W. Huang, S. K. Shaw, J. Schiffbauer, M. A. Pillers, X. Mu, S. Luo, T. Zhang, Y. Huang, G. Li, S. Ptasinska, M. Lieberman, T. Luo, *ACS Nano* **2017**, *11*, 5510.
- [16] Q. Jiang, L. Tian, K.-K. Liu, S. Tadepalli, R. Raliya, P. Biswas, R. R. Naik, S. Singamaneni, *Adv. Mater.* **2016**, *28*, 9400.
- [17] M. Zhu, Y. Li, G. Chen, F. Jiang, Z. Yang, X. Luo, Y. Wang, S. D. Lacey, J. Dai, C. Wang, C. Jia, J. Wan, Y. Yao, A. Gong, B. Yang, Z. Yu, S. Das, L. Hu, *Adv. Mater.* **2017**, *29*, 1704107.
- [18] F. Jiang, H. Liu, Y. Li, Y. Kuang, X. Xu, C. Chen, H. Huang, C. Jia, X. Zhao, E. Hitz, Y. Zhou, R. Yang, L. Cui, L. Hu, *ACS Appl. Mat. Interfaces* **2018**, *10*, 1104.
- [19] Y. Yang, R. Zhao, T. Zhang, K. Zhao, P. Xiao, Y. Ma, P. M. Ajayan, G. Shi, Y. Chen, *ACS Nano* **2018**, *12*, 829.
- [20] Y. Li, T. Gao, Z. Yang, C. Chen, W. Luo, J. Song, E. Hitz, C. Jia, Y. Zhou, B. Liu, B. Yang, L. Hu, *Adv. Mater.* **2017**, *29*, 1700981.
- [21] G. Ni, S. H. Zandavi, S. M. Javid, S. V. Boriskina, T. A. Cooper, G. Chen, *Energy Environ. Sci.* **2018**, *11*, 1510.
- [22] Z. Liu, H. Song, D. Ji, C. Li, A. Cheney, Y. Liu, N. Zhang, X. Zeng, B. Chen, J. Gao, Y. Li, X. Liu, D. Aga, S. Jiang, Z. Yu, Q. Gan, *Global Challenges* **2017**, *1*, 1600003.
- [23] V. Kashyap, A. Al-Bayati, S. M. Sajadi, P. Irajizad, S. H. Wang, H. Ghasemi, *J Mater. Chem. A* **2017**, *5*, 15227.
- [24] Q. Ma, P. Yin, M. Zhao, Z. Luo, Y. Huang, Q. He, Y. Yu, Z. Liu, Z. Hu, B. Chen, H. Zhang, *Adv. Mater.* **2019**, 1808249.
- [25] H. Song, Y. Liu, Z. Liu, M. H. Singer, C. Li, A. R. Cheney, D. Ji, L. Zhou, N. Zhang, X. Zeng, Z. Bei, Z. Yu, S. Jiang, Q. Gan, *Advanced Science* **2018**, *5*, 1800222.
- [26] Y. Shi, R. Li, Y. Jin, S. Zhuo, L. Shi, J. Chang, S. Hong, K.-C. Ng, P. Wang, *Joule* **2018**, *2*, 1171.
- [27] L. Zhou, Y. Tan, D. Ji, B. Zhu, P. Zhang, J. Xu, Q. Gan, Z. Yu, J. Zhu, *Sci. Adv.* **2016**, *2*, 1501227.
- [28] R. Hatakeyama, *Rev. Mod. Plasma Phys.* **2017**, *1*: 7.
- [29] K. Yu, G. Lu, Z. Bo, S. Mao, J. Chen, *J. Phys. Chem. Lett.* **2011**, *2*, 1556.
- [30] I. Yoshikazu, T. Yoichi, J. Han, F. Takeshi, T. Katsumi, M. Chen, *Adv. Mater.* **2015**, *27*, 4302.
- [31] Z. Bo, S. Mao, Z. J. Han, K. Cen, J. Chen, K. Ostrikov, *Chem. Soc. Rev.* **2015**, *44*, 2108.
- [32] Z. Bo, Y. Yang, J. Chen, K. Yu, J. Yan, K. Cen, *Nanoscale* **2013**, *5*, 5180.

- [33] N. Bundaleska, J. Henriques, M. Abrashev, A. M. Botelho do Rego, A. M. Ferraria, A. Almeida, F. M. Dias, E. Valcheva, B. Arnaudov, K. K. Upadhyay, M. F. Montemor, E. Tatarova, *Sci. Rep.* **2018**, *8*, 12595.
- [34] A. L. M. Reddy, A. Srivastava, S. R. Gowda, H. Gullapalli, M. Dubey, P. M. Ajayan, *ACS Nano* **2010**, *4*, 6337.
- [35] N. Soin, S. S. Roy, S. Roy, K. S. Hazra, D. S. Misra, T. H. Lim, C. J. Hetherington, J. A. McLaughlin, *J. Phys. Chem. C* **2011**, *115*, 5366.
- [36] M. Acik, Y. J. Chabal, *Jpn. J. Appl. Phys.* **2011**, *50*, 070101.
- [37] X. Gao, H. Lan, S. Li, X. Lu, M. Zeng, X. Gao, Q. Wang, G. Zhou, J.-M. Liu, M. J. Naughton, K. Kempa, J. Gao, *Global Challenges* **2018**, *2*, 1800035.
- [38] H. Li, Y. He, Y. Hu, X. Wang, *ACS Appl. Mat. Interfaces* **2018**, *10*, 9362.
- [39] S. Wu, G. Xiong, H. Yang, Y. Tian, B. Gong, H. Wan, Y. Wang, T. Fisher, J. Yan, K. Cen, Z. Bo, K. Ostrikov, *Matter* (to be published).
- [40] Q. Zhang, X. Xu, H. Li, G. Xiong, H. Hu, T. S. Fisher, *Carbon* **2015**, *93*, 659.
- [41] H. Yang, Z. Bo, J. Yan, K. Cen, *Int. J. Heat Mass Transfer* **2019**, *133*, 416.
- [42] World Health Organization, Calcium and magnesium in drinking-water: public health significance, [http://www.who.int/water\\_sanitation\\_health/publications/publication\\_9789241563550/en/](http://www.who.int/water_sanitation_health/publications/publication_9789241563550/en/), accessed: **2009**.
- [43] World Health Organization, Safe drinking-water from desalination, [http://www.who.int/water\\_sanitation\\_health/publications/desalination\\_guidance/en/](http://www.who.int/water_sanitation_health/publications/desalination_guidance/en/), accessed: **2011**.
- [44] H. Yang, J. Yang, Z. Bo, S. Zhang, J. Yan, K. Cen, *J. Power Sources* **2016**, *324*, 309.
- [45] C. Finnerty, L. Zhang, D. L. Sedlak, K. L. Nelson, B. Mi, *Environ. Sci. Technol.* **2017**, *51*, 11701.
- [46] H. Ren, M. Tang, B. Guan, K. Wang, J. Yang, F. Wang, M. Wang, J. Shan, Z. Chen, D. Wei, H. Peng, Z. Liu, *Adv. Mater.* **2017**, *29*, 1702590.
- [47] Z. Yin, H. Wang, M. Jian, Y. Li, K. Xia, M. Zhang, C. Wang, Q. Wang, M. Ma, Q.-s. Zheng, Y. Zhang, *ACS Appl. Mat. Interfaces* **2017**, *9*, 28596.

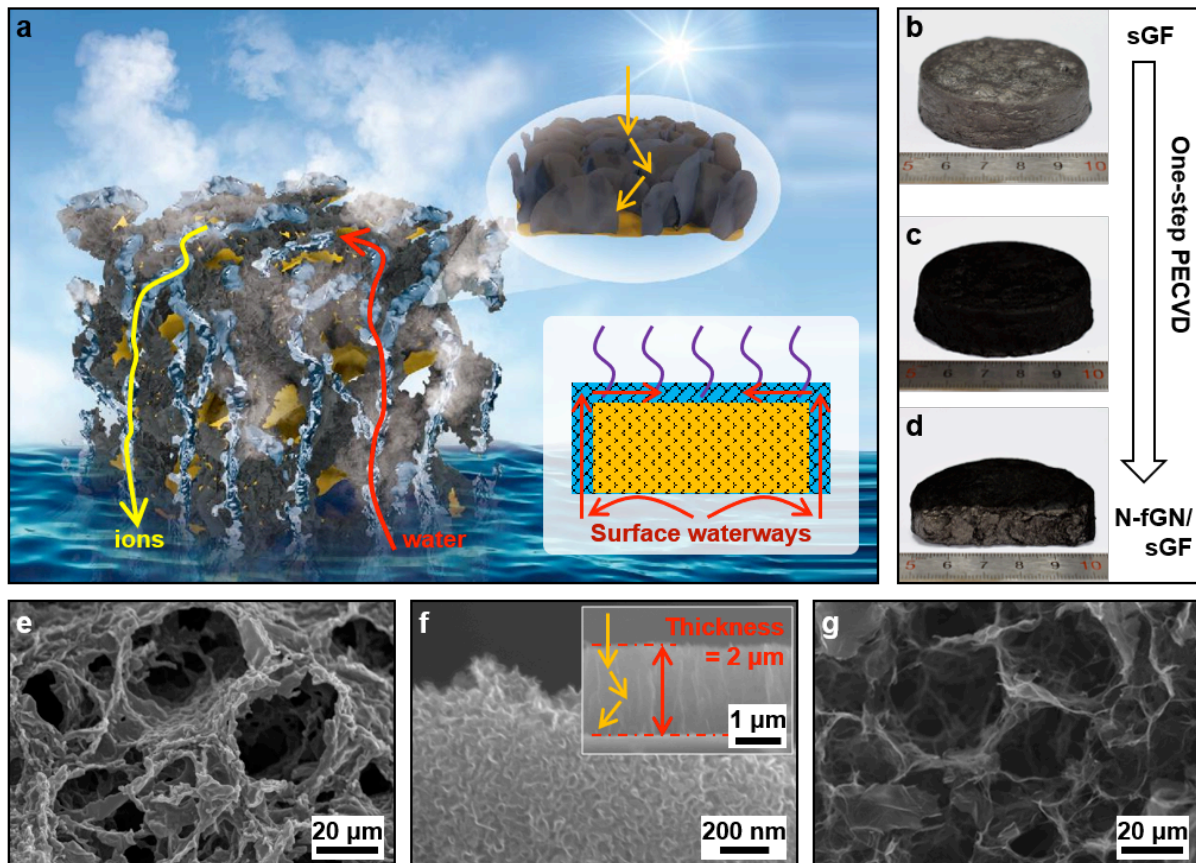


**Figure. 1** a) Schematic of the concept of on-surface waterways with a proof-of-concept N-fGN/sGF nano-architectures. b) Optical image of the sGF sample. c), d) Optical images of the N-fGN/sGF sample (c) and its section view (d). e), f) SEM images of the external surface of N-fGN/sGF. The inset of f) is the side-view, indicating the thickness of N-fGN layer. g) SEM image of the internal portion of N-fGN/sGF.

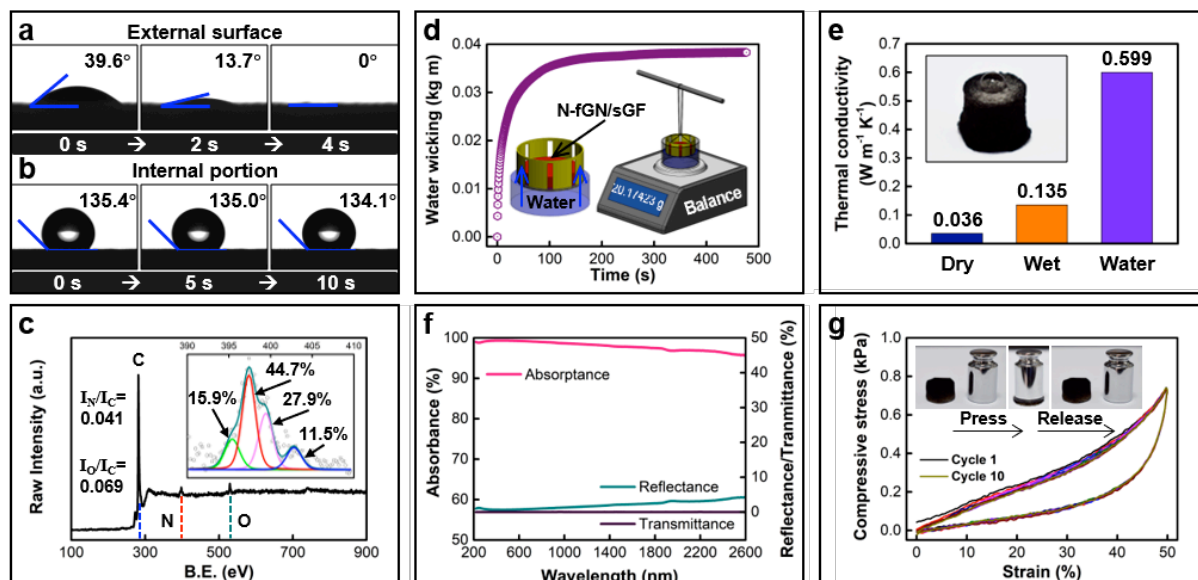


**Figure. 2** a) Water contact angle evolution of the external surface of N-fGN/sGF. b) Water contact angle evolution of the internal portion (cross-section) of N-fGN/sGF. c) XPS spectrum of the external surface of N-fGN/sGF and the Gaussian line fitted N1s spectrum (inset). d) Water wicking evolution and the experimental set-up (inset). e) Thermal conductivities of N-fGN/sGF at dry and wet states. A water droplet lies on the cross-section of N-fGN/sGF (inset). f) Optical properties including absorbance, reflectance and transmittance of N-fGN/sGF. d) Mechanical stability characterized by cyclically compressive test over 10 cycles. A N-fGN/sGF sample with a diameter of 16 mm and a thickness of 10 mm is pressed by a 50-g-weight (inset).

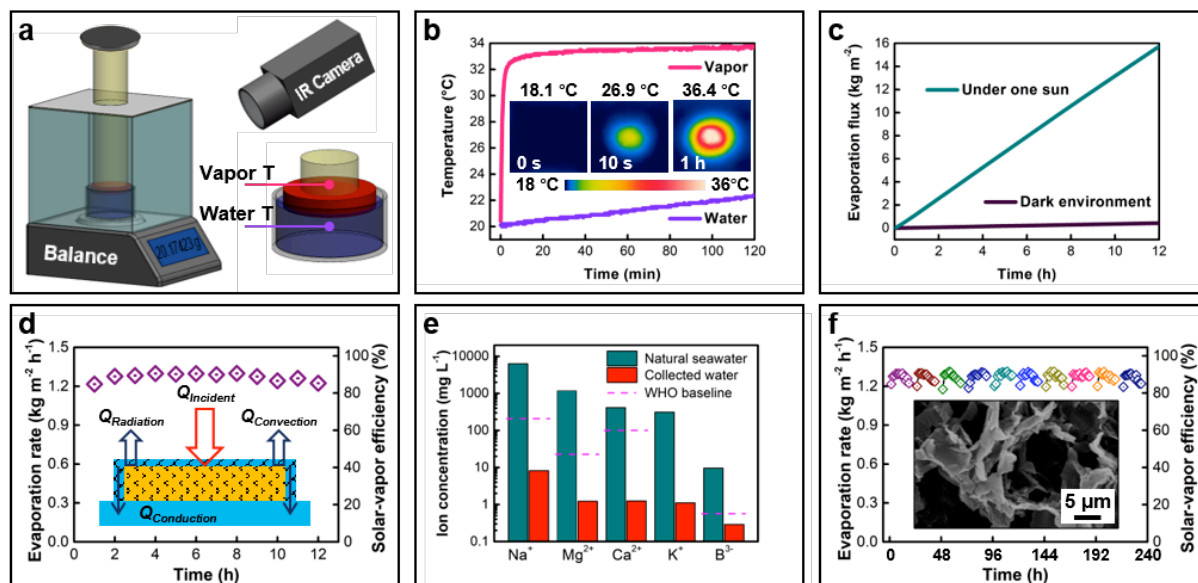


**Figure. 3** a) Experimental set-up of solar vapor generation test. Natural seawater collected from the South China Sea is used as feed. b) Temperature evolutions of hot vapor (5 mm above the top surface of sample) and bulk water (5 mm below the bottom surface of sample) recorded by thermocouples. IR images of the top surface of N-fGN/sGF recorded by IR camera (insets). c) Evaporation flux evolution under the irradiation of a normal solar density of  $1 \text{ kW m}^{-2}$  and dark environment. d) Evaporation rates and solar-vapor efficiency during consecutive operation of 12 hours. Thermal analysis (inset) for the heat loss by conduction ( $Q_{Conduction}$ ), convection ( $Q_{Convection}$ ) and radiation ( $Q_{Radiation}$ ). e) Ion concentrations of the condensed clean water compared with those in natural seawater. f) Long-term stability test over 240 hours. The SEM image of the N-fGN/sGF sample that has consecutively worked for 240 hours and then cleaned by deionized water (inset).

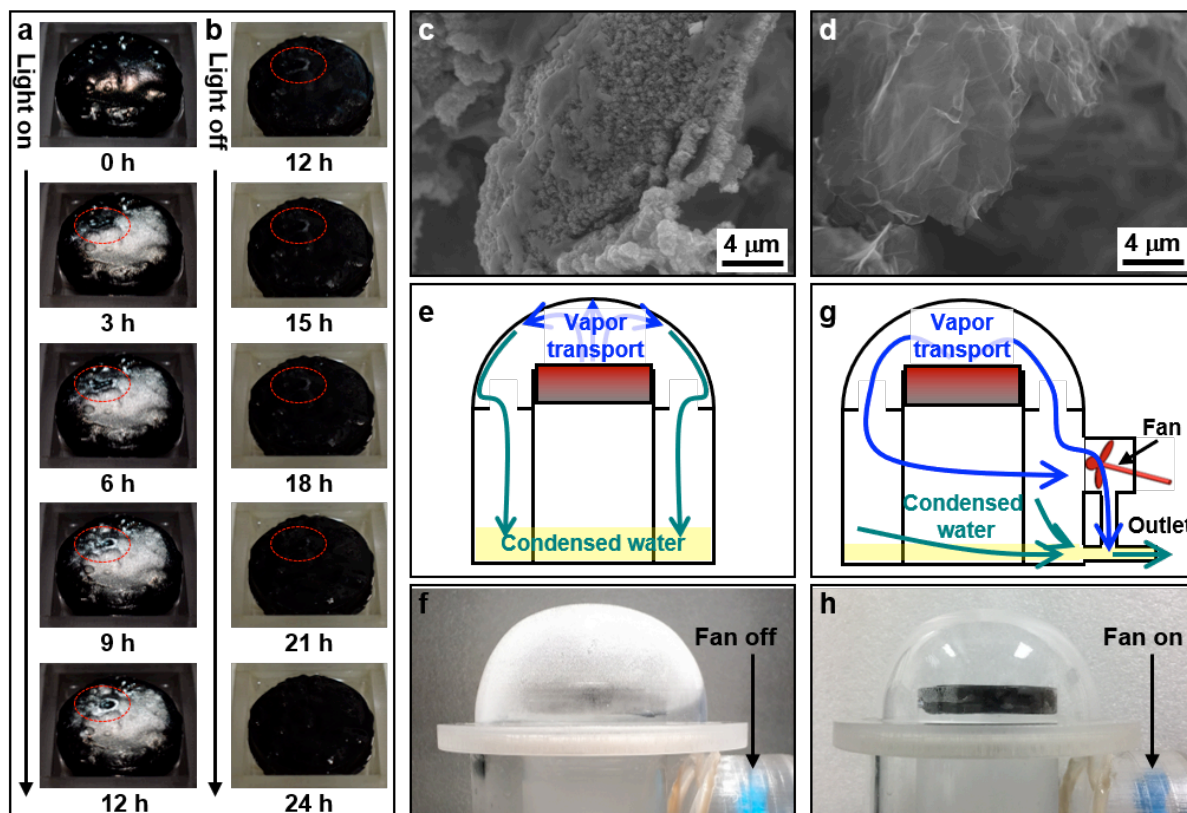


**Figure. 4** a) Optical images of salt deposition process. b) Optical images of salt diffusion process. c) SEM image of the external surface of the N-fGN/sGF sample after 12-hour operation. d) SEM image of the internal portion of the N-fGN/sGF sample after 12-hour operation. e) Schematic of vapor transport path with fan off. f) Optical image of the dome after 1-hour evaporation with fan off. g) Schematic of vapor transport path with fan on. h) Optical image of dome after 12-hour evaporation with fan on.

**Table of contents entry:**

A One-step plasma-enabled deposition is used to produce on-surface waterways by integrating hydrophilic on-surface light-absorber and hydrophobic internal thermal-insulator into a solar desalination device. The heat conduction loss is thus suppressed, leading to high solar-vapor efficiency of  $88.6 \pm 2.1\%$ , high daily evaporation yield of  $15.76 \text{ kg m}^{-2}$ , high clean

water collection ratio of 83.5%, self-cleaning and anti-salt-fouling behavior and long-term stability.

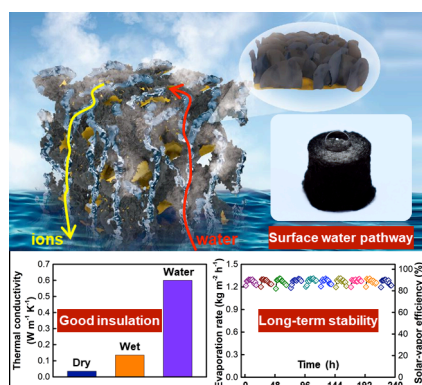
**Keywords:**

energy conversion materials, plasma nanotechnology, plasma graphene fabrication, water desalination, self-cleaning

Shenghao Wu, Guoping Xiong, Huachao Yang, Biyao Gong, Yikuan Tian, Chenxuan Xu, Yan Wang, Timothy Fisher, Jianhua Yan, Kefa Cen, Tengfei Luo, Xin Tu, Zheng Bo\* and Kostya (Ken) Ostrikov

**Multifunctional solar waterways: plasma-enabled self-cleaning nano-architectures for energy-efficient desalination**

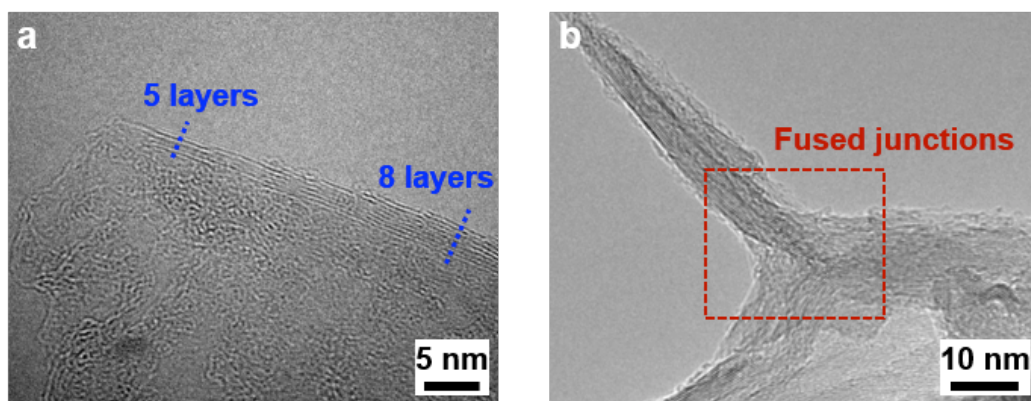
**ToC figure:**



## Supporting Information

**Multifunctional solar waterways: plasma-enabled self-cleaning nano-architectures for energy-efficient desalination**

*Shenghao Wu, Guoping Xiong, Huachao Yang, Biyao Gong, Yikuan Tian, Chenxuan Xu, Yan Wang, Timothy Fisher, Jianhua Yan, Kefa Cen, Tengfei Luo, Xin Tu, Zheng Bo\* and Kostya (Ken) Ostrikov*

**1. TEM images of N-fGNs/sGF**

**Figure S1.** a) TEM image of a single plasma-made graphene nanopetal with 5-8 graphitic layers. b) TEM image of the N-fGNs-sGF interface connected by fused junction.



## 2. Water contact angle measurement under irradiation

The water contact angle of the N-fGN/sGF sample is measured under the irradiation with a normal solar density of  $1 \text{ kW m}^{-2}$ . As shown in Figure S2a, when a water droplet interacts with the external surface, it quickly permeates into the sample, which is consistent with the result observed under normal laboratory room illumination (see Figure 2a in the main text). This result indicates that the external surface maintains the hydrophilic property when placed under solar irradiation.

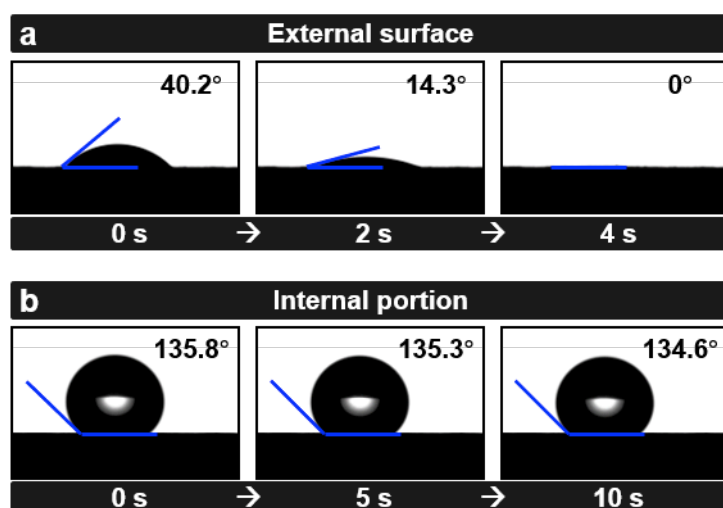


**Figure S2.** a) Water contact angle evolution of the external surface of N-fGN/sGF sample under the irradiation with a normal solar density of  $1 \text{ kW m}^{-2}$ . b) Water contact angle evolution of the internal portion (cross-section) of N-fGN/sGF sample under the irradiation with a normal solar density of  $1 \text{ kW m}^{-2}$ .

On the other hand, when a water droplet is dropped on the internal portion (cross-section), it maintains the high contact angle, as shown in Figure S2b. This result is consistent with the test performed without irradiation (see Figure 2b in the main text). Thus, the wetting property of the internal portion of N-fGN/sGF sample is also well-preserved upon irradiation.

### 3. Stability test of nitrogenated/oxygenated groups

As shown in Figure S3, the atom ratios of nitrogen to carbon ( $I_N/I_C$ ) and oxygen to carbon ( $I_O/I_C$ ) are measured to be 0.041 and 0.069, respectively, in the original N-fGN/sGF. After 10 cycles (240 h) of the solar desalination process, the  $I_N/I_C$  and  $I_O/I_C$  are measured to be 0.039 and 0.070, respectively. The atom ratios are very close to the original ones. Thus, the nitrogenated/oxygenated groups are stable when the samples are exposed to saline water.

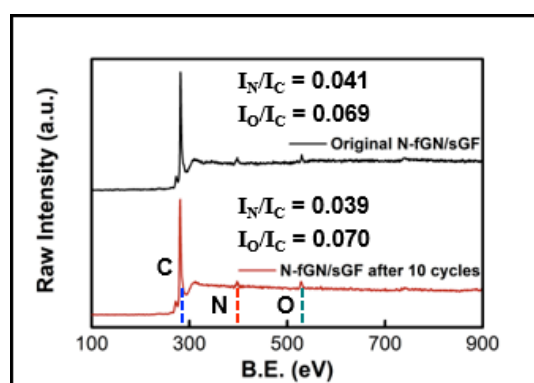


**Figure S3.** XPS spectra of the original N-fGN/sGF sample and the sample after the consecutive solar desalination process of 10 days. Note that the latter sample was cleaned by deionized water after the solar desalination process.

### 4. Experimental set-up of water wicking test

As shown in Figure S4a, the N-fGNs/sGF sample with a diameter of 40 mm is placed in a supporter. The supporter is composed of metal mesh through which water can easily flow. The metal supporter is tied to a holder, which is movable. A beaker containing water is placed on a precise balance with an accuracy of 0.01mg. When the supporter containing a N-fGNs/sGF sample is putted on the top surface of water, the mass of beaker will immediately increase due to the buoyancy. Subsequently, the mass measured by the balance gradually decreases, as shown in Figure S4b, because that water is adsorbed by the N-fGNs/sGF sample,

leading to the decreased buoyancy and reduced water in the beaker. It's worth noting that mass change measured by balance is twice as much as the water mass adsorbed by the N-fGNs/sGF sample. As such, the water wicking by the N-fGNs/sGF sample is obtained by dividing the as-measured mass change by 2. Note that when the water wicking reach 95% of the average value during 300 to 480 s, it can be considered as the saturated state.

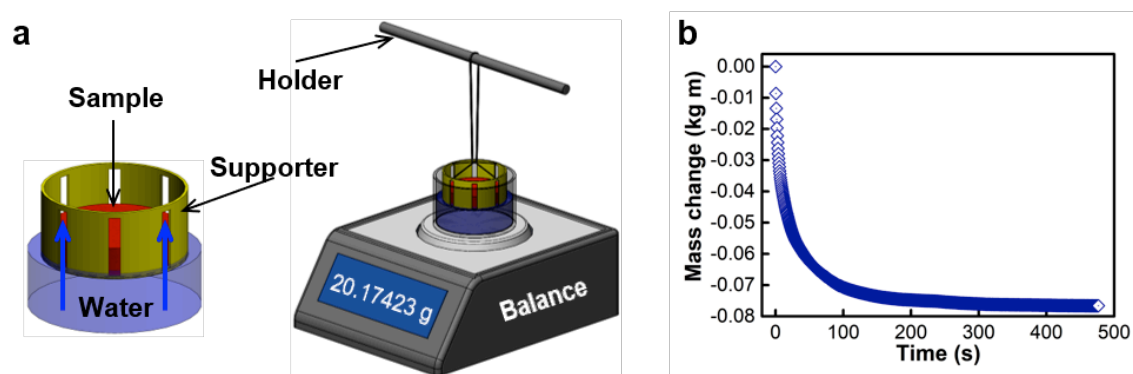


**Figure S4.** Experimental set-up of water wicking test

## 5. Superiority of the surface waterway design over previous materials.

**Table S1.** Comparison of evaporation performance with previous studies at 1 sun.

Light absorber	Optical absorbance	Thermal insulator	Conductivity ( $\text{W m}^{-1} \text{K}^{-1}$ )		Evaporation rate ( $\text{kg m}^{-2} \text{h}^{-1}$ )	Solar-vapor efficiency
			Dry state	Wet state		
Exfoliated graphite <sup>[S1]</sup>	97%, 250~2,250 nm	Carbon foam	0.117	0.426	1.0 *	66.0%
Gold membranes <sup>[S2]</sup>	91%, 400~2,500 nm	/	/	/	0.6	48.0% *
Al nanoparticles membrane <sup>[S3]</sup>	96%, 400~2,500 nm	/	/	/	0.9 *	57.0% *
Gold-deposited nanoporous template <sup>[S4]</sup>	99%, 400 nm~10 $\mu\text{m}$	/	/	/	1.0 *	64.0% *
Carbon nanotube membrane <sup>[S5]</sup>	98%, 200~800 nm	/	/	/	1.32	82.0%
Hierarchical graphene foam <sup>[S6]</sup>	95% at visible, 90% at near infrared	/	/	/	1.4	91.4%
Carbon nanotube/graphene oxide <sup>[S7]</sup>	97%, 250~1,200 nm	Graphene oxide/nanofibrillated cellulose	0.06	0.13	1.25	85.6%
Mushroom <sup>[S8]</sup>	96%, 200~2,500 nm	/	0.45	/	1.277	78.0%
Carbon nanotube <sup>[S9]</sup>	97%, 300~1,200	Cellulose nanofibrils	0.06	/	1.11	76.3%
Flame-treated wood <sup>[S10]</sup>	97%, 780~2,500 nm	Wood	0.33	/	1.05	72.0%
Graphene foam <sup>[S11]</sup>	97%, 200~2,500 nm	Graphene foam	0.016	0.45	1.3	87%
Carbonized wood <sup>[S12]</sup>	99%, 250~2,500 nm	Wood	0.2	/	0.83	57.3%
Activated carbon fiber <sup>[S13]</sup>	94%, 300~2,500 nm		0.095	0.430	1.22	79.4%
Carbonized wood <sup>[S14]</sup>	95%, 300~2,500 nm	Wood	0.11	0.14	1.08	74.0%
Charcoal <sup>[S15]</sup>	87~98%, 300~2,500 nm	Polyvinyl alcohol sponge	0.193	0.457	1.15*	73%
<b>N-fGNs (Current work)</b>	<b>98%, 200~2,600 nm</b>	<b>sGF</b>	<b>0.036</b>	<b>0.135</b>	<b>1.27±0.03</b>	<b>88.6±2.1%</b>

\* Estimated from plots in literatures;

The existing conjugated structures are composed by a top light-absorbing layer and a bottom thermal-insulating layer, as shown in Figure S5a. Light-absorbing materials (e.g., graphene oxide, carbonized wood, charcoal and activated carbon) are usually coated on the top surface of thermal-insulating materials (e.g., bacterial nanocellulose, natural wood, polyvinyl alcohol sponge and activated carbon fiber felt) and often show smooth transition/conjunction between the layers. Since the thermal-insulating layer lies between the light-absorbing layer and the underneath water, these insulating materials have to be hydrophilic. Only when the underneath water flow through the thermal-insulating layer, it can reach the top light-absorbing layer and then evaporates. This top-down structure suffers from a drawback that the thermal-insulating efficacy will be dramatically reduced when the thermally conductive water fills the porosity of the insulator and serves as heat-losing paths. As a result, the intrinsically low thermal conductivities of the insulating materials in the previous works increase from 0.069, 0.34, 0.193 and 0.095  $\text{W m}^{-1} \text{K}^{-1}$  to 0.466, 0.38, 0.457 and 0.430  $\text{W m}^{-1} \text{K}^{-1}$ , respectively, when impregnated with water. These thermal conductivities during practical desalination are very close to the thermal conductivity of bulk water (0.59  $\text{W m}^{-1} \text{K}^{-1}$ ), leading to the loss of the thermal-insulating efficacy.

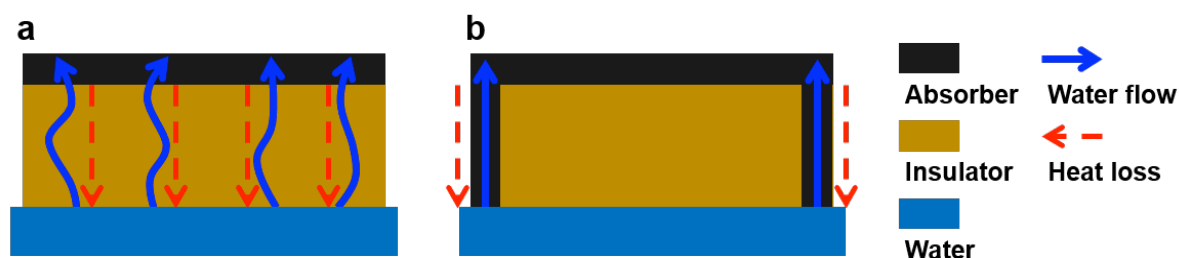


**Figure S5.** a) The conjugated structure in previous works. b) The conjugated structure with surface waterways in the current work.

On the contrary, in our surface waterways design, the hydrophilic light-absorbing material is seamlessly coated on the external surface of the hydrophobic thermal-insulating material, as shown in Figure S5b. The light-absorbing material can also serve as waterways while the thermal-insulating material prevents the infiltration of water. Consequently, the heat-losing paths caused by the water filling the porosity of insulator can be efficiently eliminated, leading to less heat loss from the top absorber to the underneath bulk water. As shown in Table. R1, the thermal conductivity ( $0.135 \text{ W m}^{-1} \text{ K}^{-1}$ ) of our N-fGN/sGF sample slightly increases when working on water, compared with that at dry state ( $0.036 \text{ W m}^{-1} \text{ K}^{-1}$ ). Nevertheless, the value is still far smaller than that of water ( $0.59 \text{ W m}^{-1} \text{ K}^{-1}$ ). The change of thermal conductivity ( $0.099 \text{ W m}^{-1} \text{ K}^{-1}$ ) from the dry state to wet state is much smaller than those of previous works ( $0.397$ ,  $0.264$  and  $0.335 \text{ W m}^{-1} \text{ K}^{-1}$ ). The well-preserved insulating efficacy will benefit the solar desalination performance. Based on the thermal analysis in Figure 3d of the revised Manuscript, the heat loss from the top absorber to the underneath water is reduced to 3.0%.

## 6. Roles of plasma in the synthesis

### *i) Growing fGNs to obtain improved light absorption*

The plasma process enabled surface nano-structuring for solar energy harvesting. Indeed, the N-fGNs grown on the external surface of sGF show vertical orientation in arrays (see the SEM images in Figure 1e and 1f of the main text), which can effectively trap light. As shown in Figure S6a, the light absorbance is dramatically increased after the plasma nanostructuring process. The average light absorbance of N-fGN/sGF is measured to be 98.0%, which is much higher than the bare sGF (73.9%). The plasma-nanostructuring-enhanced light absorption is one of the key factors for the ultimate performance of solar vapor generation.

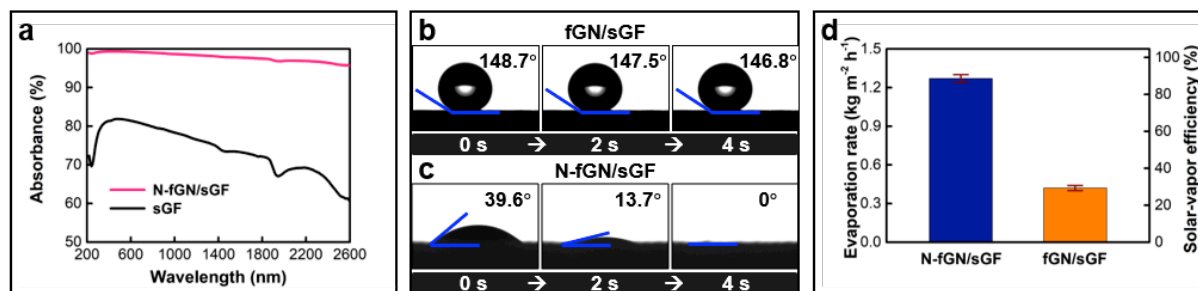


**Figure S6.** a) Light absorbance before (sGF, black line) and after (N-fGN/sGF, red line) PECVD process. b) Wetting behavior of N-fGN/sGF sample with N-doping. c) Wetting behavior of fGN/sGF sample without N-doping. d) Solar vapor performance of N-fGN/sGF and fGN/sGF sample.

### *ii) Doping nitrogen species to obtain hydrophilic wettability*

In addition, the wetting behavior is important for water supply and interfacial heat transfer. By introducing nitrogenated species into the frameworks of fGNs via plasma doping, the surface wettability of the sample is changed from hydrophobic to hydrophilic. As shown in Figure S6b, the pristine graphene structure (fGN/sGF) fabricated by the PECVD process (where only CH<sub>4</sub> and H<sub>2</sub> are used as the precursors) are super-hydrophobic by nature. When NH<sub>3</sub> is introduced during the PECVD process, the wettability of N-fGN/sGF changes to be hydrophilic due to the N-doping effect, as shown in Figure S6c.

### *iii) Functionalize the nanoarchitectures to obtain surface waterways*

For comparison, a solar vapor test for pristine fGN/sGF is conducted. As shown in Figure S6d, the energy efficiency of fGN/sGF is measured to be 29.5±1.4%, which is much lower than that of N-fGN/sGF (88.6±2.1%). This result demonstrates the importance of the plasma-doping-enabled waterways for the ultimate performance of solar vapor applications.

## 7. Thermogravimetry Analysis

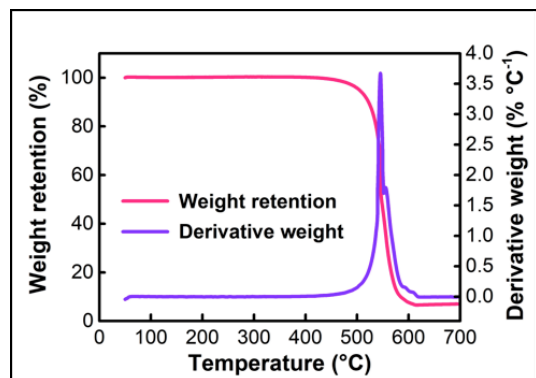


**Figure S7.** Thermogravimetry curve (red) and derivative thermogravimetry curve (purple).

## 8. Clarification of the water-free sGF layer

A long-time test of water contact angle of the sGF layer (i.e., the cross-section of N-fGN/sGF) is conducted. As shown in Figure S8a, the initial water contact angle is recorded to be  $135.6^\circ$ , suggesting the hydrophobic wetting property. Then, the contact angle is nearly unchanged from 1 min to 1 h. Besides, when a water droplet is placed on the cross-section of N-fGN/sGF, the droplet cannot infiltrate into the internal portion of N-fGN/sGF, as shown by the inset of Figure S8b. The results confirm that the sGF layer can prevent water infiltration.

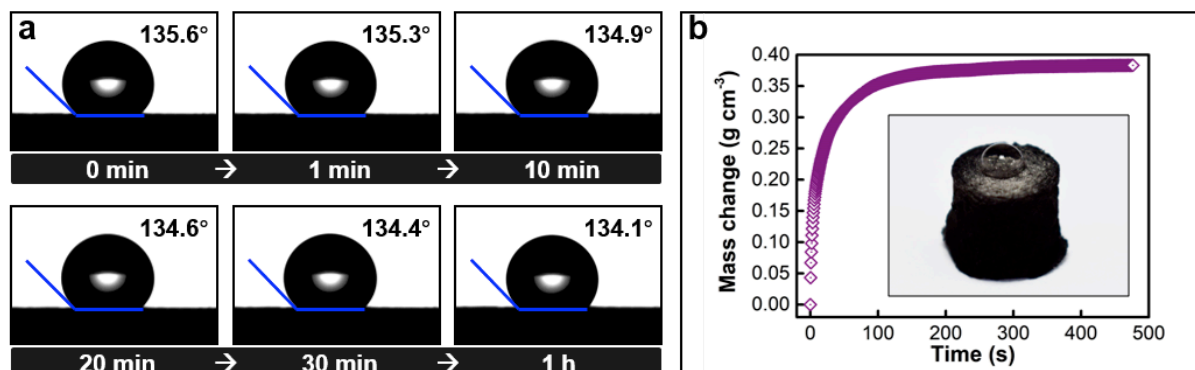


**Figure S8.** a) Wetting behavior of the sGF layer (i.e., the internal portion of N-fGN/sGF). b) Mass change of N-fGN/sGF when half-immersed in water. A sample with a diameter of 4 cm



and a thickness of 1 cm is used. The inset present that a water droplet is placed on the sGF layer.

The mass change (or water adsorption) is measured when the N-fGN/sGF is submerged in water. The method has been presented in Figure S4. As shown in Figure S8b, the mass change gradually increases as time evolves because the water is adsorbed by the N-fGN/sGF sample. The mass change eventually falls at  $0.38 \text{ g cm}^{-3}$ , which is much smaller than the mass density of pure water ( $1.0 \text{ g cm}^{-3}$ ). If the porosity of sGF layer is filled with water, the mass change should be close to  $1.0 \text{ g cm}^{-3}$ . Thus, this result also suggests that water cannot fill the internal porous space of the N-fGN/sGF sample.

## 9. Analysis of heat transfer processes

Thermal analysis for the solar vapor desalination process is conducted, including the effective energy for evaporation ( $Q_{Evap}$ ), conductive heat loss to bulk water ( $Q_{Conduction}$ ), convective ( $Q_{Convection}$ ) and radiative ( $Q_{Radiation}$ ) heat loss to the surroundings.

**The energy dynamic equilibrium** can be expressed as:

$$A \alpha q_{Solar} = Q_{Evap} + Q_{Conduction} + Q_{Convection} + Q_{Radiation} \quad (S1)$$

, where  $A$  denotes the surface area of absorber facing the sun,  $\alpha$  solar absorbance, and  $q_{Solar}$  input solar flux.<sup>[S16]</sup>

**The effective energy for evaporation ( $Q_{Evap}$ )** can be calculated as:

$$Q_{Evap} = m_{evap} (h_{lv} + C (T_v - T_l)) \quad (S2)$$

, where  $m_{evap}$  is evaporation rate ( $1.27 \text{ kg m}^{-2} \text{ h}^{-1}$ ),  $h_{lv}$  is latent heat of liquid-vapor phase change ( $2,453.3 \text{ kJ kg}^{-1}$  at  $33.6^\circ\text{C}$ ),  $C$  is specific heat of water ( $4.2 \text{ kJ kg}^{-1} \text{ K}^{-1}$ ),  $T_v$  is vapor

temperature (33.6°C), and  $T_l$  is water temperature (22.4 °C). Consequently, the  $Q_{Evap}$  is calculated to be 886.2 J m<sup>-2</sup>, corresponding 88.6%.

**The conductive heat loss to bulk water ( $Q_{Conduction}$ )** can be calculated through the temperature gradient in the underlying water:

$$Q_{Conduction} = A k (T_{l1} - T_{l2}) / \Delta l \quad (S3)$$

, where  $k$  denotes thermal conductivity of bulk water.<sup>[S1]</sup> The temperature gradient in the underlying water below the samples is measured by two embedded thermocouples (i.e.,  $T_{l1}$ = 22.4 °C and  $T_{l2}$ = 21.9 °C). The distance between the thermocouples  $\Delta l$  is 10 mm. Consequently, the  $Q_{Conduction}$  is calculated to be 30.0 J m<sup>-2</sup>, corresponding 30.0%

**The convective heat loss ( $Q_{Convection}$ )** to the adjacent environment can be calculated as:

$$Q_{Convection} = A h (T_a - T_\infty) \quad (S4)$$

, where  $h$  is convection heat transfer coefficient (assumed to be 10 W m<sup>-2</sup> K<sup>-1</sup>),  $T_a$  is the top surface temperature of absorber (36.4°C), and  $T_\infty$  is the temperature of the adjacent environment. Since the light-absorbing material is surrounded by water layer and hot vapor, the adjacent temperature can be approximated as the vapor temperature (i.e.,  $T_\infty = T_{vapor}$ =33.6°C). Consequently, the  $Q_{Convection}$  is calculated to be 28.0 J m<sup>-2</sup>, corresponding 2.8%

**The radiative heat loss ( $Q_{Radiation}$ )** to the ambient environment can be calculated as:

$$Q_{Radiation} = A \varepsilon \sigma (T_a^4 - T_{ambient}^4) \quad (S5)$$

, where  $\varepsilon$  denotes the emission of the absorber (assumed to be 0.98), and  $\sigma$  is the Stefan-Boltzmann constant (5.669×10<sup>-8</sup> W m<sup>-2</sup> k<sup>-4</sup>).

Currently, controversies exist in the state-of-the-art literatures concerning the ambient temperature  $T_{ambient}$  in determining radiative heat losses. Some believe that the ambient temperature can be approximated as the temperature at the infinity (i.e.,  $T_{ambient} = 20^{\circ}\text{C}$  in this work),<sup>[S11]</sup> and others believe that because of the existence of water layers and hot vapor above the light-absorbing material, the ambient temperature can be approximated as the vapor temperature (i.e.,  $T_{ambient} = T_{vapor} = 33.6^{\circ}\text{C}$ ).<sup>[S18]</sup> Since water and vapor is semitransparent to thermal radiation, we believe that the two currently prevailing viewpoints on the choice of ambient temperature values set the upper and lower limits; therefore, the radiative heat loss should fall within the range that are delimited by the maximum and minimum values calculated by using  $T_{\infty} = T_{ambient}$  and  $T_{\infty} = T_{vapor}$ , respectively.

When  $T_{ambient} = 20^{\circ}\text{C}$ , the radiative heat loss is calculated as  $99.7 \text{ W m}^{-2}$ , corresponding to 10%. When  $T_{ambient} = T_{vapor} = 33.6^{\circ}\text{C}$ , the radiative heat loss is calculated as  $18.2 \text{ W m}^{-2}$ , corresponding to 1.8%. Therefore, the radiative heat loss in this work falls in the range of 1.8~10%.

## 10. Raman spectra of N-fGNs/sGF

A typical Raman spectrum of the top surface of N-fGNs/sGF is presented in Figure S9. The D peak located at  $\sim 1331 \text{ cm}^{-1}$  is resulted from various types of defects and the exposed edges.<sup>[S19]</sup> The G peak rising at  $\sim 1563 \text{ cm}^{-1}$  is attributed to the in-plane  $sp^2$  phonon vibration.<sup>[S20]</sup> The intensity ratio of the D to G ( $I_D/I_G$ ) related to the disorder degree and the in-plane crystalline size is calculated as 1.36, suggesting the existence of a large number of edges, some defects and disorder in the  $sp^2$  graphene structure. The 2D peak located at  $\sim 2664 \text{ cm}^{-1}$  is sensitive to the number of layers of graphene. The broad 2D peak and the  $I_{2D}/I_G$  ratio

of 0.36 indicate that the plasma-made graphene nanopetals are consisted of few graphitic layers.<sup>[S21]</sup>

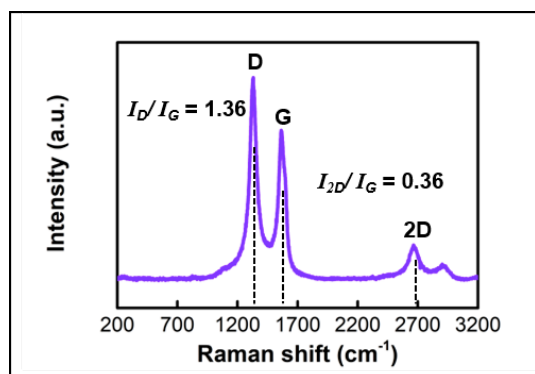


**Figure S9.** Raman spectrum of the top surface of N-fGNs/sGF.

### 11. Morphology after solar desalination process

The morphology of the N-fGN/sGF sample is characterized after 10 cycles of solar desalination process. As shown in Figure S10a, the morphology of the external surface does not show any observable difference from the original state (please see the SEM images in Figure 1e and 1f of the revised Manuscript). The N-fGNs are uniformly coated on the frameworks of sGF. These results confirm that the hierarchical structure at the external surface of N-fGN/sGF sample is well-preserved during the solar desalination process.

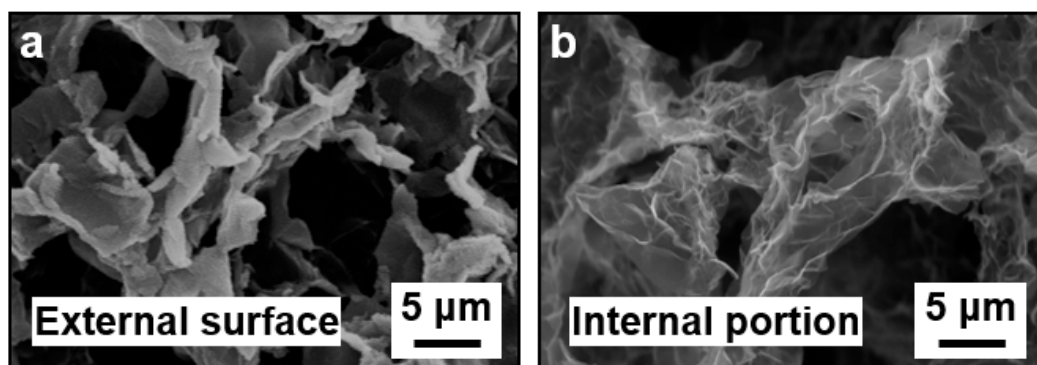


**Figure S10.** SEM images of the a) external surface and b) internal portion of the N-fGN/sGF sample after 12 cycles of solar desalination process. Note that the sample was cleaned by deionized water and dried before the SEM detection.

On the other hand, the morphology of the internal portion of N-fGN/sGF sample after 10 cycles of the solar desalination process is shown in Figure S10b. It is observed that the porosity of the sGF frameworks is well-maintained during the solar desalination process.

## 12. Solar vapor performance vs saline concentration

As shown in Figure S11, three levels of saline concentration are chosen for the test, in which the 3.25 wt% is corresponding to the natural seawater from the South China Sea, and the 6.5 wt% is two-fold of the natural seawater when the 16.25 wt% is five-fold. It is observed that the evaporation rate decreases when the saline concentration increases. The evaporation rate at 3.25 wt% of salty is measured to be  $1.27 \pm 0.03 \text{ kg m}^{-2} \text{ h}^{-1}$ , corresponding to  $88.6 \pm 2.1\%$  of energy efficiency. When the saline concentration increases to 6.5 wt%, the evaporation rate and energy efficiency decrease to  $1.24 \pm 0.05 \text{ kg m}^{-2} \text{ h}^{-1}$  and  $86.4 \pm 3.5\%$ , respectively. When the saline concentration increases to 16.25 wt%, the evaporation rate and energy efficiency further decrease to  $1.21 \pm 0.04 \text{ kg m}^{-2} \text{ h}^{-1}$  and  $84.1 \pm 2.8\%$ , respectively. Thus, to obtain stable performance, the water in the desalination device should be periodically renewed to avoid the increase the saline concentration.

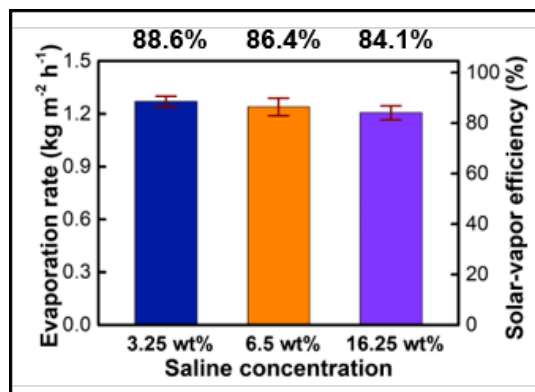


**Figure S11.** Solar desalination performance under the salty from 3.25 wt% (natural seawater from the South China Sea) to 16.25 wt% (five-fold of natural seawater).

The saline concentration of the water will increase when the device works. The increasing saline concentration will reduce the speed of ion diffusion and reduce the self-cleaning effect. One possible solution is to renew the water avoiding the increase of the saline level. As such, a water flow design is necessary to ensure the self-cleaning behavior. In the current work, we employ a water peristaltic pump to renew the water in the desalination device.

### 13. The effect of the thickness of N-fGNs on solar vapor performance

We have tuned the growth time of N-fGNs to obtain different thicknesses of the N-fGN layer. Typical SEM images of the N-fGN layer are shown in Figure S12a and S12b. For all cases, the thickness of sGF is chosen as 1 cm. As shown in Figure S12a, when the N-fGN growth time is set as 30 min, a thickness of 0.9  $\mu\text{m}$  is obtained, corresponding to the N-fGN to sGF thickness ratio of 1 : 11,111. As shown in Figure S12b, when the growth time is set as 60 min, a thickness of 2.0  $\mu\text{m}$  is obtained, corresponding to the N-fGN to sGF thickness ratio of 1 : 5,000.

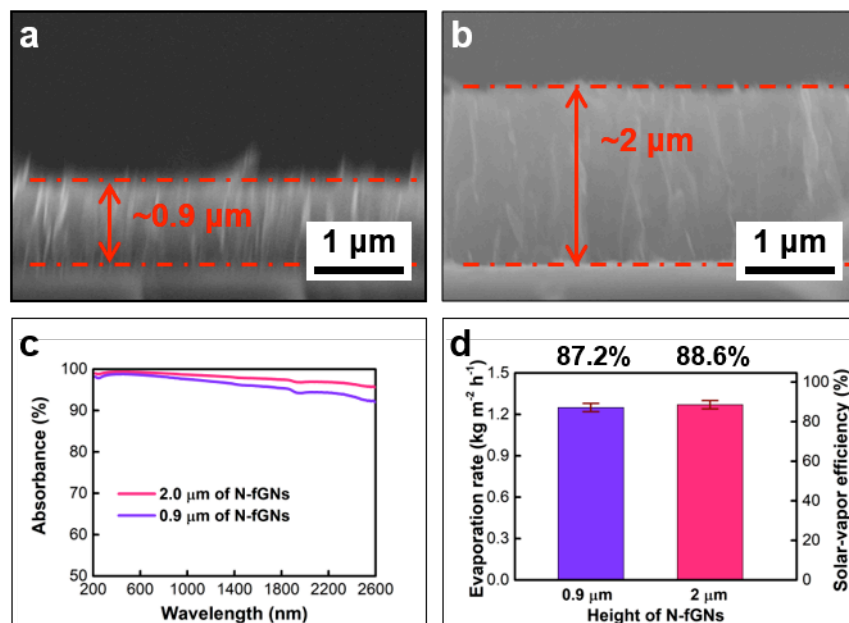


**Figure S12.** a) SEM image of the section-view of the N-fGN layer grown by 30 min of PECVD process. The thickness of N-fGN layer is observed to be 0.9 μm. b) SEM image of the section-view of the N-fGN layer grown by 60 min of PECVD process. The thickness of N-fGNs is observed to be 2 μm. c) The light absorbance across the wavelength of 200 to 2,600 nm of the N-fGN/sGF sample fabricated by 30 min (purple line) and 60 min (red line) of PECVD process. d) Comparison of solar performance with different N-fGN thickness of 0.9 μm and 2.0 μm.

The light absorbance of the samples was also measured. As shown in Figure S12c, increasing the thickness of the N-fGN layer from 0.9 μm to 2.0 μm slightly increases absorbance across the wide wavelength range of 200 to 2,600 nm. The average light absorbance of the 2.0-μm-N-fGN/sGF sample is calculated to be 98.0%, which is higher than that of the 0.9-μm-N-fGN/sGF sample (96.2%). This result demonstrates that increasing the thickness of the N-fGN layer (or increasing the thickness ratio of N-fGN to sGF) can improve light absorption.

The samples were subsequently used for solar vapor tests at 1 sun. As shown in Figure S12d, the evaporation rate of the 0.9- $\mu\text{m}$ -N-fGN/sGF sample is measured to be  $1.25\pm 0.03 \text{ kg m}^{-2} \text{ h}^{-1}$ , corresponding to an energy efficiency of  $87.2\pm 2.1\%$ . On the other hand, the evaporation rate of the 2.0- $\mu\text{m}$ -N-fGN/sGF sample is measured to be  $1.27\pm 0.03 \text{ kg m}^{-2} \text{ h}^{-1}$ , corresponding to an energy efficiency of  $88.6\pm 2.1\%$ . It was observed that increasing the thickness of N-fGN layer (or the thickness ratio of N-fGN to sGF) can slightly increase the evaporation rate and the energy efficiency, although the effect falls within experimental uncertainties.

As such, the solar performance may be further improved by increasing the thickness of the N-fGN layer (or the thickness ratio of N-fGN to sGF), but any improvement would be limited because the solar performance in the current work is already high. Meanwhile, further prolonging the growth time of N-fGNs to increase the thickness will result in higher costs of energy and gas precursors. Thus, for the current work, further increasing the thickness of the N-fGN layer does not seem to be necessary.

#### **14. The effect of the thickness of N-fGNs on self-cleaning behavior**

The self-cleaning behavior of the N-fGN/sGF samples with different thickness ratios of N-fGN to sGF has been tested under the irradiation with a normal solar density of  $1 \text{ kW m}^{-2}$ . The results for the 0.9- $\mu\text{m}$ -N-fGN/sGF sample is shown in Figure S13. The time sequence of images reveals that the salt accumulates within the first 12 hours when the light is turned on. Then, the salt residues gradually dissolve and eventually disappear after 21-24 h when the light is turned off.



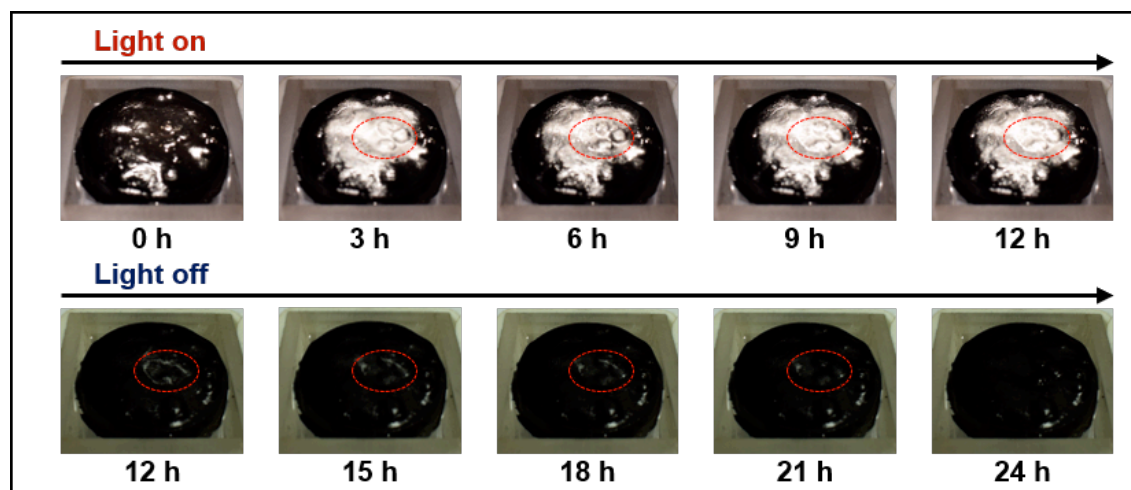


**Figure S13.** The test of self-cleaning behavior of the 0.9 μm N-fGN/sGF sample.

On the other hand, the result for the 2.0-μm-N-fGN/sGF sample is shown in Figure S14. The salt also accumulates within the first 12 hours and gradually dissolves within the latter 12 hours. Compared with the 0.9-μm-N-fGN/sGF sample, the salt residing on the top surface of the 2.0-μm-N-fGN/sGF sample is less pronounced at the 21<sup>st</sup> hour. The salt residue almost completely dissolves into bulk liquid at the 21<sup>st</sup> hour.

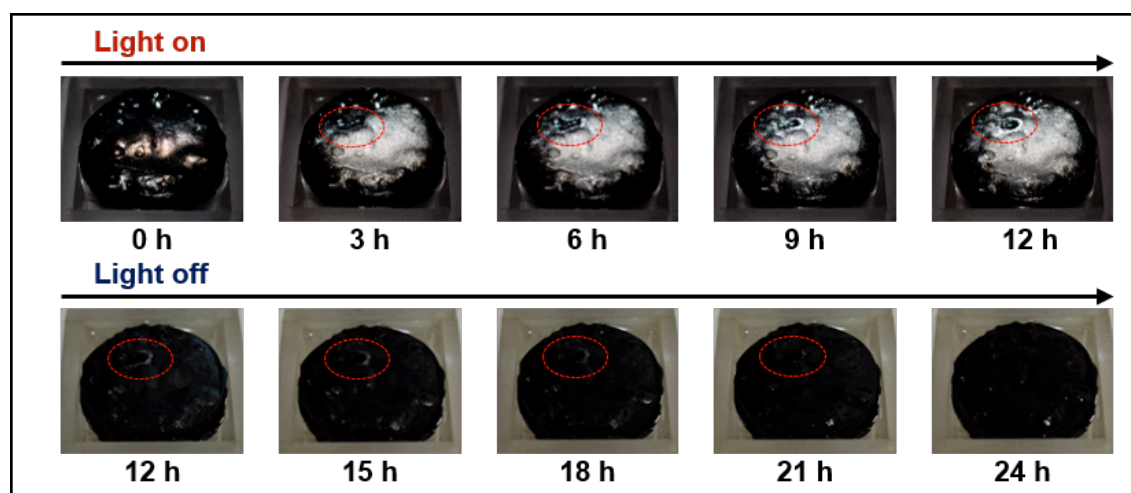


**Figure S14.** The test of self-cleaning behavior of the 2.0 μm N-fGN/sGF sample.

These results indicate that increasing the thickness of N-fGN layer may slightly accelerate the self-cleaning speed, but any improvement is limited. As discussed in the main text of the paper, the thickness of the N-fGN layer (0.9-2.0  $\mu\text{m}$ ) is so small compared with the thickness of the surface water layer (several microns to millimeters). The speed of salt diffusion might be mainly determined by the thickness of the surface water layer instead of the thickness of the N-fGN layer. Since the self-cleaning ability in the current work has satisfied the requirement of solar desalination (self-cleaning at night time), it does not appear to be really necessary to further increase the thickness of the N-fGN layer.

## References

- [S1] H. Ghasemi, G. Ni, A. M. Marconnet, J. Loomis, S. Yerci, N. Miljkovic, G. Chen, *Nat. Commun.* **2014**, *5*, 4449.
- [S2] K. Bae, G. Kang, S. K. Cho, W. Park, K. Kim, W. J. Padilla, *Nat. Commun.* **2015**, *6*, 10103.
- [S3] L. Zhou, Y. Tan, J. Wang, W. Xu, Y. Yuan, W. Cai, S. Zhu, J. Zhu, *Nat. Photonics* **2016**, *10*, 393.
- [S4] L. Zhou, Y. Tan, D. Ji, B. Zhu, P. Zhang, J. Xu, Q. Gan, Z. Yu, J. Zhu, *Sci. Adv.* **2016**, *2*, 1501227.
- [S5] Y. Wang, L. Zhang, P. Wang, *ACS Sustain. Chem. Eng.* **2016**, *4*, 1223.
- [S6] H. Ren, M. Tang, B. Guan, K. Wang, J. Yang, F. Wang, M. Wang, J. Shan, Z. Chen, D. Wei, H. Peng, Z. Liu, *Adv. Mater.* **2017**, *29*, 1702590.
- [S7] Y. Li, T. Gao, Z. Yang, C. Chen, W. Luo, J. Song, E. Hitz, C. Jia, Y. Zhou, B. Liu, B. Yang, L. Hu, *Adv. Mater.* **2017**, *29*, 1700981.
- [S8] N. Xu, X. Hu, W. Xu, X. Li, L. Zhou, S. Zhu, J. Zhu, *Adv. Mater.* **2017**, *29*, 1606762.
- [S9] F. Jiang, H. Liu, Y. Li, Y. Kuang, X. Xu, C. Chen, H. Huang, C. Jia, X. Zhao, E. Hitz, Y. Zhou, R. Yang, L. Cui, L. Hu, *ACS Appl. Mat. Interfaces* **2018**, *10*, 1104.
- [S10] G. Xue, K. Liu, Q. Chen, P. Yang, J. Li, T. Ding, J. Duan, B. Qi, J. Zhou, *ACS Appl. Mat. Interfaces* **2017**, *9*, 15052.
- [S11] Y. Yang, R. Zhao, T. Zhang, K. Zhao, P. Xiao, Y. Ma, P. M. Ajayan, G. Shi, Y. Chen, *ACS Nano* **2018**, *12*, 829.
- [S12] M. Zhu, Y. Li, G. Chen, F. Jiang, Z. Yang, X. Luo, Y. Wang, S. D. Lacey, J. Dai, C. Wang, C. Jia, J. Wan, Y. Yao, A. Gong, B. Yang, Z. Yu, S. Das, L. Hu, *Adv. Mater.* **2017**, *29*, 1704107.
- [S13] H. Li, Y. He, Y. Hu, X. Wang, *ACS Appl. Mat. Interfaces* **2018**, *10*, 9362.
- [S14] H. Liu, C. Chen, G. Chen, Y. Kuang, X. Zhao, J. Song, C. Jia, X. Xu, E. Hitz, H. Xie, S. Wang, F. Jiang, T. Li, Y. Li, A. Gong, R. Yang, S. Das, L. Hu, *Adv. Energy. Mater.* **2018**, *8*, 1701616.
- [S15] X. Gao, H. Lan, S. Li, X. Lu, M. Zeng, X. Gao, Q. Wang, G. Zhou, J.-M. Liu, M. J. Naughton, K. Kempa, J. Gao, *Global Challenges* **2018**, *2*, 1800035.
- [S16] Q. Jiang, L. Tian, K.-K. Liu, S. Tadepalli, R. Raliya, P. Biswas, R. R. Naik, S. Singamaneni, *Adv. Mater.* **2016**, *28*, 9400.

- [S17] G. Ni, G. Li, S. V. Boriskina, H. Li, W. Yang, T. Zhang, G. Chen, *Nat. Energy* **2016**, *1*, 16126.
- [S18] Z. Yin, H. Wang, M. Jian, Y. Li, K. Xia, M. Zhang, C. Wang, Q. Wang, M. Ma, Q.-S. Zheng, Y. Zhang, *ACS Appl. Mat. Interfaces* **2017**, *9*, 28596.
- [S19] R. P. Vidano, D. B. Fischbach, L. J. Willis, T. M. Loehr, *Solid State Commun.* **1981**, *39*, 341.
- [S20] F. Tuinstra, J. L. Koenig, *J. Chem. Phys.* **1970**, *53*, 1126.
- [S21] A. C. Ferrari, J. C. Meyer, V. Scardaci, C. Casiraghi, M. Lazzeri, F. Mauri, S. Piscanec, D. Jiang, K. S. Novoselov, S. Roth, A. K. Geim, *Phys. Rev. Lett.* **2006**, *97*, 187401.